

Contents lists available at ScienceDirect

Transportation Research Part E

journal homepage: www.elsevier.com/locate/tre





Post-earthquake building damage assessment: A multi-period inspection routing approach for Gaussian process regression

Yinhu Wang a,*, Amirhossein Cheraghi b, Ge Ou b, Nikola Marković a

- ^a Department of Civil and Environmental Engineering, University of Utah, USA
- ^b Department of Civil and Coastal Engineering, University of Florida, USA

ARTICLE INFO

Keywords:
Intelligent disaster management
Building damage inspection
Multi-period routing optimization
Lagrangian relaxation
Gaussian process regression

ABSTRACT

In the wake of seismic events, prompt and accurate building damage assessment is crucial to inform post-disaster interventions and recovery efforts. This paper advances a novel multiperiod planning strategy for post-earthquake building inspections, conceptualizing the task as a multi-period orienteering problem (MPOP). In this framework, each building selected for inspection hosts a specific reward indicating its informative value for damage assessment. The objective is to design inspection routes that maximize damage information acquisition while adhering to time constraints. After data collection, we utilize a Gaussian process regression (GPR) model to estimate the damage in uninspected buildings. To validate our approach, we conduct an earthquake simulation with realistic building information from San Francisco. The experimental outcomes reveal that our multi-period damage assessment framework maintains robust performance across diverse scenarios and consistently surpasses conventional period-by-period inspection strategies, yielding enhanced damage information acquisition and greater precision in damage estimation. This outcome underscores the effectiveness of our proposed method in strengthening post-earthquake damage assessment and improving recovery planning.

1. Introduction

Earthquakes are common and devastating natural disasters that frequently occur worldwide (Farooqui et al., 2017). These seismic events often cause extensive damage to both human lives and man-made infrastructure (Frolova et al., 2017; Dong and Shan, 2013). After an earthquake, performing a prompt assessment of building damage in the affected region is an imperative task. To guarantee the precision of building damage information, on-site inspections are regarded as a dependable approach where skilled professionals are dispatched to the affected buildings to meticulously assess the earthquake-induced damage. These field surveys facilitate a thorough damage assessment, thereby assisting in well-informed decision-making regarding post-earthquake recovery.

In practice, time and resource constraints limit inspections to all affected buildings within a region. To address this, the research community advocates for the use of "representative samples". Using this approach, specific building samples are inspected to train a damage inference model. Subsequently, this model is utilized to estimate damages for the remaining uninspected buildings (Sheibani and Ou, 2021; Stojadinović et al., 2022; Mangalathu and Jeon, 2020). Emphasizing efficient sampling, Sheibani and Ou (2021) proposed a clustering method where a building from each cluster acts as a representative data point, reflecting the characteristics of other buildings within its cluster. This clustering-based approach has received affirmation in subsequent studies for enhancing sampling efficiency and improving the performance of learning algorithms (Demir et al., 2010; Wu, 2018; Liu and Wu, 2020).

^{*} Corresponding author.

E-mail addresses: yinhu.wang@utah.edu (Y. Wang), a.cheraghi@ufl.edu (A. Cheraghi), gou@ufl.edu (G. Ou), nikola.markovic@utah.edu (N. Marković).

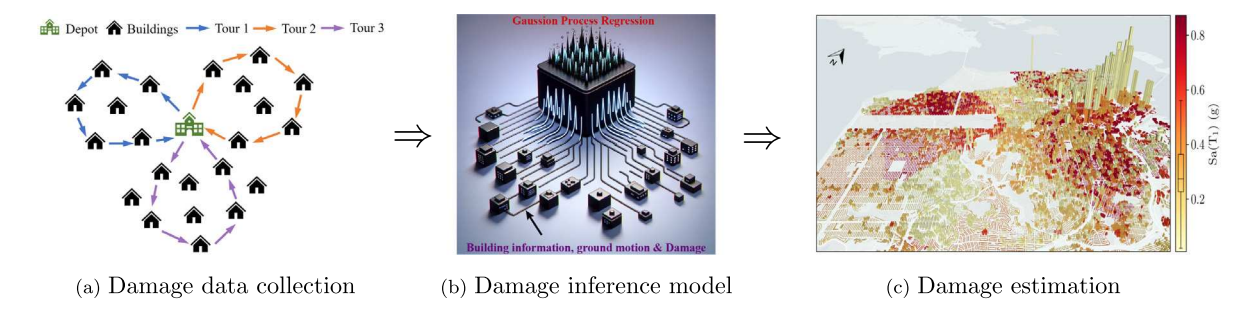


Fig. 1. A multi-period inspection-based framework for post-seismic regional building damage inference.

Due to constraints imposed by daily working hours, comprehensive building inspections usually extend for multiple periods. Consequently, it becomes imperative to improve the efficiency of inspection routing and make the best use of the available time to conduct inspections for more damage information. Some of the related work formulates the inspection routing problem as a traveling salesman problem or a vehicle routing problem in which all inspections are conducted within one or multiple trips with a minimum travel distance or time (Lagaros and Karlaftis, 2011). In actuality, inspecting all representative buildings can be impossible due to strict inspection schedules. To work within these time constraints while maximizing damage data collection, some research suggests adopting a selective inspection approach to gather as much damage data as possible (Cheraghi et al., 2024). This strategy frames the inspection routing problem for each period as an orienteering problem, emphasizing the optimization of routes based on immediate objectives for that specific period. While this period-by-period approach seems effective, it carries the risk of becoming overly focused on local optimization and potentially missing out on a more globally efficient routing planning.

Departing from this convention, our study introduces a multi-period inspection routing approach. This method embraces a broader perspective, aiming to maximize damage information collection across multiple periods to conduct regional building damage estimation (see Fig. 1). In this framework, we begin by employing a clustering algorithm to sample a set of representative buildings. Each of these selected buildings is then assigned a non-negative reward based on a tailored reward assignment criterion. Consequently, we determine multi-period inspection routes maximizing reward collection while adhering to daily and cumulative working-hour constraints. Using the building damage data gathered from inspections along these optimized routes, we proceed to train a damage inference model to estimate the damage in uninspected buildings within an earthquake-affected region.

Our main contributions focus on:

- An advanced method for post-earthquake damage assessment that combines optimization of inspection routing with machine learning.
- A fresh perspective on inspection routing, turning it into an MPOP, offering a viable alternative to the conventional period-by-period approach.
- The introduction of a Lagrangian relaxation method addresses the challenges of routing planning over multiple periods. Paired with a Gaussian process regression (GPR) model, this aids in making accurate damage estimations in uninspected buildings.
- Method validation on instances with real-world building information data from San Francisco, showing the superiority of our multi-period inspection routing model. In our tests, our approach performs better than the conventional period-by-period inspection planning, both in terms of reward gain and damage estimation accuracy.

2. Literature review

This section reviews the literature on post-earthquake building damage assessment using diverse data sources, optimizing inspection routes for on-site building damage assessment, and routing optimization involving multi-period planning.

2.1. Post-earthquake building damage assessment

2.1.1. Image-based damage assessment

Remote sensing technologies provide access to satellite imagery, enabling extensive coverage for rapid seismic building damage assessment. Leveraging these images, extensive research integrates computer vision and machine learning to detect earthquake-induced damage effectively. Ji et al. (2018) develop a convolutional neural network for identifying building collapses, employing high-resolution satellite images from the 2010 Haiti earthquake. Similarly, Xia et al. (2023) train a convolutional neural network using high-resolution remote sensing images of buildings before and after the 2023 Turkey earthquake, subsequently applying the network to assess the extent of building damage in Islahiye. Additional research on post-earthquake damage assessment using remote sensing images includes studies by Wu et al. (2014), Cha et al. (2018), Chen and Yu (2019), Xu et al. (2019), Ma et al. (2020), Qing et al. (2022), Xu et al. (2023a), Cui et al. (2022), Wang et al. (2022) and Wang et al. (2023c).

While the aforementioned research extensively utilizes remote sensing images for post-earthquake damage assessment, it is noteworthy that most remote sensing images provide only a top-down view of buildings, thus limiting the assessment of facade damage and other structural details. This constraint significantly affects the depth of damage assessment for impacted buildings. With the advancement of unmanned aerial vehicle (UAV) technologies, they are increasingly recognized for their capability to collect comprehensive damage data, including information on facades and ground floors (Levine and Spencer, 2022; Xu et al., 2023b). Contributions to seismic damage assessment using UAV-captured images include works by Wang et al. (2023b), Xiong et al. (2020), and Han et al. (2022). Despite UAVs provide detailed insights into building structural conditions, their limitations in navigating tight spaces may omit crucial information on non-structural elements and occupancy status, such as gas leaks or hazardous substances. Additionally, varying UAV flight regulations across jurisdictions pose challenges for their universal application after seismic events (Franke et al., 2018).

Current research on image-based damage assessment mainly offers a basic classification of damage levels, with limited quantitative analysis of building damage. To improve post-earthquake rescue and relief operations, it is crucial to develop a comprehensive framework that enables a more accurate evaluation of building damage.

2.1.2. Crowdsourcing-based damage assessment

Crowdsourcing platforms leverage eyewitness reports, offering a swift means to estimate the extent of damage. Pioneering this initiative, the United States Geological Survey introduced the "Did You Feel It?" online platform in 1999. This platform was designed to collect seismic intensity data and related damage reports from internet users, processing and archiving this information based on postal zip codes. Subsequently, these data are used to generate interactive maps (Quitoriano and Wald, 2020).

On the technological front, recent advances in natural language processing enable researchers to acquire earthquake-induced damage information from textual data. In their investigation, Madichetty and Sridevi (2019) use statistical features of tweets, such as hashtag frequency and mentions, and keywords pertinent to infrastructure and casualties, to detect damage-related tweets for the 2015 Nepal earthquake. Xing et al. (2021) employ a character-level convolutional neural network trained using crowdsourced social media and mobile phone signaling data to estimate the impact of the 2017 Jiuzhaigou earthquake.

Although crowdsourcing offers a cost-effective means to gather damage data, its dependency on subjective input and susceptibility to data biases diminish its reliability for precise damage estimations. For example, factors such as population density and internet accessibility influence its reach and representativeness, potentially skewing the data in favor of regions with denser populations or greater internet penetration (Li et al., 2023; Quitoriano and Wald, 2020). Therefore, crowdsourcing is viewed as a complementary tool to other methods, such as remote sensing and on-site inspections, which provide finer detail and precision in damage assessment.

2.1.3. Damage assessment through on-site inspection

On-site inspection typically involves trained professionals meticulously evaluating buildings, and providing detailed quantitative assessments of structural changes due to earthquake-induced ground motions. Although time-consuming and resource-intensive, on-site inspection is a reliable method for precise damage assessment. After the L'Aquila earthquake on 6 April 2009, over 70,000 buildings were inspected for seismic performance analysis (Indirli et al., 2013). In the aftermath of the 2015 Gorkha earthquake, more than 30,000 paper assessment forms were utilized to evaluate the safety and damage of residential buildings in the impacted regions (Didier et al., 2017).

To enhance on-site inspection efficiency and seek accurate damage estimation across affected regions, a method integrating selective inspections and machine learning is proposed. This involves focusing on carefully selecting representative buildings. The damage data gathered from the inspections on these buildings is then utilized to train a machine learning model, enabling the estimation of damage in the remaining uninspected buildings. Sheibani and Ou (2021) and Stojadinović et al. (2022) leverage k-means clustering to identify a minimal subset of buildings for damage inspection. Wieland et al. (2012) initially categorizes the entire building population into distinct sub-populations and then utilize a random sampling approach to select representative buildings. Tamang et al. (2023) introduce a stratified purpose sampling technique to select a representative set of samples. In our work, we apply a k-means clustering algorithm used in the work by Sheibani et al. (2022) to group all the buildings into distinct clusters, and from each cluster, one building is selected as a representative building to be potentially inspected.

Supervised learning techniques have shown that building damage in uninspected structures can be reliably estimated using data from a small subset of inspected buildings (Kovačević et al., 2018; Kourehpaz and Molina Hutt, 2022). These methods typically involve training a damage estimation model using collected damage data and subsequently applying the trained model to assess damage in uninspected buildings. Various supervised learning algorithms have been employed to predict seismic damage on a regional scale. For instance, studying the 2015 Nepal earthquake, which resulted in over \$7 billion in damage and loss, Ghimire et al. (2022) compare a set of algorithms including linear regression, support vector regression, and gradient boosting. They find that the random forest regression outperforms the others in terms of predictive accuracy. Mangalathu et al. (2020) analyze building damage data from the 2014 Napa, CA earthquake, revealing that random forest algorithms deliver superior accuracy on the specific case.

While ensemble methods such as random forest have demonstrated effectiveness in predicting damage, the uncertainty in predictions from ensemble tree-based models relies on the variability among weak learners, specifically decision trees (Coulston et al., 2016). In contrast, GPR models stand out due to their ability to quantify prediction uncertainties analytically by capturing distributions over predicted outputs (Schulz et al., 2018). This potentially informs decision-making by providing confidence levels for damage predictions in uninspected buildings. The non-parametric nature of GPR models allows for flexible data fitting without imposing strict assumptions about damage patterns (Williams and Rasmussen, 2006). Their proficiency in delivering dependable predictions in post-disaster scenarios has established their significance in regional building damage assessment (Sheibani and Ou, 2021; Sheibani et al., 2022; Bodenmann et al., 2023; Cheraghi et al., 2024). Recognizing the strengths of GPR in this domain, we choose it for our work on post-earthquake damage estimation.

2.2. On-site inspection route optimization

Designing efficient inspection routes, considering time constraints, to collect damage data from identified representative buildings is a critical yet underexplored aspect within the framework of damage assessment through on-site inspection. Wieland et al. (2012) treat the task of visiting all representative buildings as a Traveling Salesman Problem, aiming to minimize both costs and time spent in the field. Similarly, Nagasawa et al. (2021) determine traveling paths for a fleet of UAVs to implement post-disaster building inspections by solving a generalization of the Traveling Salesman Problem. Yet, due to realistic time constraints, it is often infeasible to inspect all representative buildings within a single trip. On the contrary, Sheibani et al. (2022) acknowledge these time constraints and adopt a day-by-day inspection strategy, iteratively training a GPR model until reaching a desired accuracy. However, a notable drawback of this method is its day-to-day focus, which tends to optimize inspection routes in isolation rather than as a coordinated sequence.

Oruc and Kara (2018) propose a bi-objective mathematical model to optimize routes for drones and motorcycles inspecting population centers and road segments in Istanbul's Kartal district in Turkey. The first objective maximizes the value added by assessing road segments, while the second maximizes the profit from inspecting points of interest. Wang et al. (2023a) formulate a D-optimal orienteering problem to identify the optimal inspection route, aiming to maximize the quality of damage information obtained from the surveyed buildings. The proposed model is optimally solved using both row-generation and column-generation techniques. The focus of both references is exclusively on optimizing the inspection routes for a single period.

2.3. Multi-period routing optimization

Our research focuses on multi-period routing optimization, a topic that has been extensively explored in existing literature. Neves-Moreira et al. (2020) propose a multi-period VRP considering refueling decisions to minimize fuel consumption costs. Dayarian et al. (2016) tackle a real-world production collection issue with demand fluctuations across periods, formulating it as a multi-period VRP to devise a tactical routing plan ensuring given levels of service quality. Zhang et al. (2024) introduce a multi-period VRP with time windows for drug distribution during epidemics, aiming to minimize total travel time and psychological penalty costs for affected areas.

Larrain et al. (2019) address a multi-period VRP with delivery due dates, where each customer is associated with a release and due date indicating goods availability and visit deadline. Using a variable MIP neighborhood descent algorithm, they aim to minimize distribution costs and delays. Laganà et al. (2021) tackle multi-period routing for postal services, proposing an adaptive large neighborhood search heuristic to minimize routing costs. Qin et al. (2015) propose a multi-period inspector scheduling problem and develop a tabu search heuristic to optimize routes for professional inspectors conducting on-site inspections at supplier factories before shipment.

Kundu et al. (2022) offer a comprehensive review of literature on disaster logistics management, highlighting a significant emphasis on single-period planning for disaster relief operations within the domain. However, the exploration of multi-period planning studies in disaster management remains limited. Sadeghi et al. (2023) develop a multi-period VRP aimed at optimizing water delivery in post-disaster humanitarian logistics. Additionally, de Castro Pena et al. (2023) propose a multi-period routing problem for cleaning debris following disasters.

In our study, we consider an inspection routing problem spanning multiple periods to conduct building damage assessment following an earthquake. The problem is formulated as a multi-period orienteering problem aiming to optimize inspection routes to maximize the accumulation of cumulative damage information. The strategic route planning across multiple periods, as opposed to the period-by-period routing approach commonly used in existing studies, enables more efficient utilization of time resources and holds the potential to increase both the total number of inspections conducted and the amount of collected damage data. Consequently, it can lead to improved damage estimation based on the data gathered during inspections.

3. Experimental data and reward assignment

In this section, we first introduce the experimental data generated through the simulation of a hypothetical earthquake scenario, utilizing realistic building information from the San Francisco Bay area testbed. Since the damage inspection routing in our work is formulated as a multi-period orienteering problem, the reward for each inspection becomes an indispensable input. As a result, we proceed to determine reward association in building inspection.

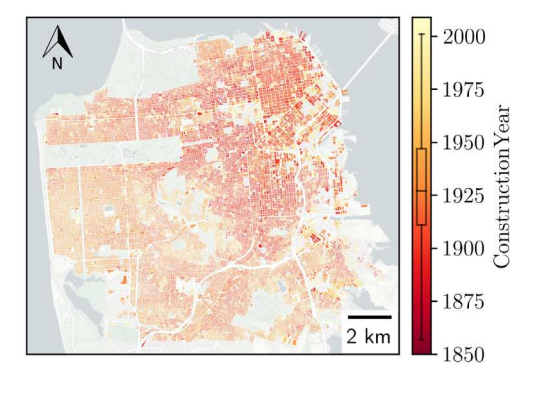
3.1. Earthquake simulation

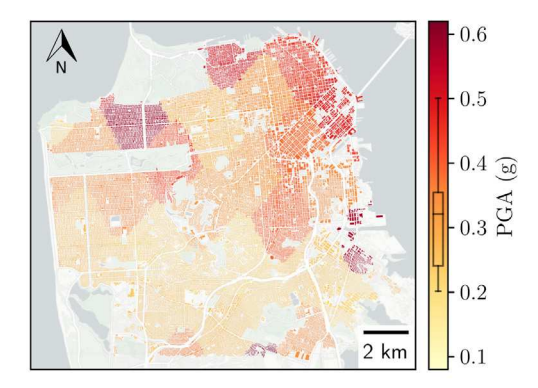
We simulate a synthetic earthquake scenario using the regional Workflow for Hazard And Loss Estimation (rWHALE) (Elhaddad et al., 2019; Lu et al., 2020). This scenario replicates an earthquake event with a magnitude of 7.0 along the Hayward fault, with its epicenter in Oakland, CA. The ground motions are generated from physics-based models based on the SW4 finite difference program (Petersson and Sjogreen, 2017), developed by Lawrence Livermore National Laboratory (Rodgers et al., 2020).

Thirty-nine simulated seismograms are evenly distributed across the region, which are subsequently assigned to individual buildings using the k-dimensional tree algorithm (Elhaddad et al., 2019). These ground motion time histories are then applied to shear building models (Lu and Guan, 2017), constructed based on building data sourced from UrbanSim (Waddell, 2002) and the testbed provided by NHERI SimCenter (Zsarnóczay et al., 2023) available at the DesignSafe data repository (Rathje et al., 2017).

Table 1
Building attributes and ground motion indices.

Building attributes	Ground motion indices
Construction year	Sa(T ₁)
No. of stories	Arias
Floor area	Fajfar
Occupancy type	Spectrum intensity
Latitude	Signal IQR
Longitude	Signal kurtosis





(a) Construction year

(b) Peak ground accelerations

Fig. 2. Geospatial distribution of building characteristics and ground motions in the San Francisco testbed: (a) by construction year and (b) by assigned peak ground accelerations (PGAs) from a grid of seismograms.

To address the inherent uncertainty in the building models, we randomize the structural characteristics such as the story height, initial stiffness, and damping ratio. Through time history analysis, we calculate engineering demand parameters, including maximum acceleration, inter-story drift ratio, and residual drift. The economic loss estimation is then carried out using the method proposed by Zeng et al. (2016) based on FEMA-P58 (FEMA, 2019). The loss ratio is a measure of repair-to-replacement costs, with a value of one indicating total loss.

3.2. Dataset characteristics

For predicting building damage, supervised learning models utilize paired input-output data. Sheibani and Ou (2021) demonstrate that a synergistic combination of readily available building attributes and specific ground motion (GM) indices aptly characterizes building inventory data for regional damage and loss predictions via a GPR model.

This study identifies several intensity measures that have a robust correlation with structural damage. Among these are the spectral acceleration at the structure's fundamental period ($Sa(T_1)$), the Arias intensity (Arias, 1970), Fajfar intensity (Fajfar et al., 1990), and spectrum intensity (Housner, 1952). Moreover, the dataset incorporates statistical attributes of GMs in the time domain, such as the Interquartile Range (IQR) and kurtosis.

Table 1 presents the set of 12 features that combine building attributes with GM characteristics. Additionally, the economic loss ratio values derived from simulations are used as damage observations, serving as the labels for the dataset. Fig. 2 displays the distribution of construction years of buildings and the peak ground acceleration represented as a fraction of the gravitational acceleration. Meanwhile, Fig. 3 provides a visual depiction of building heights proportional to the number of stories, along with spectral acceleration, $Sa(T_1)$, serving as an intensity metric that accommodates the attributes of GMs and structural properties.

In our study, we randomly select 20,000 buildings from the testbed, dividing them evenly into two sets: S and S'. The former serves as the data pool for representative sampling for on-site inspection, while the latter is exclusively reserved for evaluating the proposed damage inference framework.

3.3. Representative building selection and inspection reward allocation

This section describes our procedure for identifying representative buildings from S using clustering techniques and assigning each an inspection reward, which is instrumental for damage inspection routing.

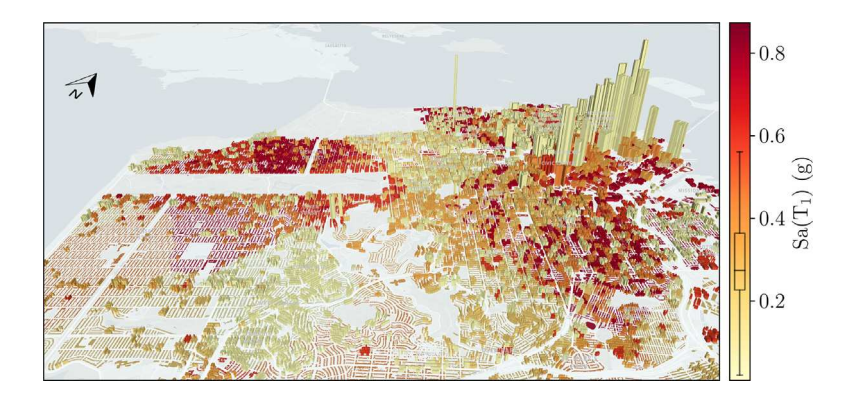


Fig. 3. Spectral acceleration Sa(T1) of buildings in the San Francisco testbed, with building heights scaled in proportion to the number of stories.

We employ a clustering approach to group analogous building data and minimize inter-group overlap, aiming to derive distinct centroids from the dataset S (Ezugwu et al., 2020). A detailed exploration of inspection reward allocation can be found in Appendix A. Let $C_i \subset S$ denote the ith cluster. The clustering objective can be formalized as:

$$\min_{\substack{\{\mu_1, \mu_2, \dots, \mu_k\} \\ \{C_1, C_2, \dots, C_k\}}} \; \sum_{i=1}^k \sum_{x \in C_i} \|x - \mu_i\|^2$$

where μ_i represents the centroid of the *i*th cluster, and *k* is the total number of clusters. This objective seeks to minimize the variance within clusters, ensuring that the chosen centroids are truly representative. Utilizing the *k*-means++ algorithm (Arthur and Vassilvitskii, 2006), we determine these centroids, and the buildings closest to them are selected as candidates for inspection, forming the subset $V \subset S$. Next, with each building $i \in V$, we associate an inspection reward

$$r_i = |\mathcal{C}_i|$$
,

which is equivalent to the size of the cluster to which building *i* belongs.

The described reward assignment is aligned with the findings of Wu (2018) and Liu et al. (2021), who introduce clustering-based sampling techniques for training regression models. They show that the centroids of larger clusters provide more representative samples, thus enhancing predictive accuracy. Sheibani et al. (2022) also validate this insight within the context of GPR, emphasizing the efficacy of selecting representative samples from sizable clusters.

4. Post-earthquake building inspection routing problem

The preceding section outlines the methodology for identifying representative buildings and assigning inspection rewards. With these rewards in place, our focus now shifts to the challenge: optimizing inspection routes to maximize total rewards over multiple periods while satisfying time constraints. Subsequent subsections present the mathematical formulation of the multi-period building inspection routing problem and offer a comprehensive discussion of the solution approaches employed to address this problem.

4.1. Mathematical formulation

The multi-period inspection routing problem can be formulated as a multi-period orienteering problem (MPOP), which is characterized by a graph denoted as G = (V, A), where the node set is defined as $V = \{0\} \cup V_c$. Here, node 0 serves as the starting and ending node of a tour, while $V_c = \{1, 2, \dots, N\}$ represents the set of buildings to be visited, at most once, across all defined periods. Each node $i \in V_c$ is associated with a reward r_i and an inspection time e_i . The reward assigned to $i \in V_c$ is determined based on the criterion outlined in Section 3.3. Notably, the reward and inspection time for node 0 are set to zero. The arc set A represents the paths connecting any adjacent pair of buildings, with each arc $a_{ij} \in A$ having an associated travel time c_{ij} .

A feasible tour within any period $t \in \{1, 2, ..., T\}$ starts and ends at node 0, and its duration cannot exceed the maximum daily working duration H. Across all periods, the cumulative working time, including time for inspection and travel, must fall within the maximum time duration denoted with W. We introduce a binary variable z_{ij}^t , equal to 1 if node j is visited immediately after node i in the tour for period t, and 0 otherwise. With these notations in place, the MPOP can be formally represented as:

$$\max_{z_{ij}^t \in \{0,1\}, u_i \in \mathbb{Z}^+} \quad \sum_{t=1}^T \sum_{i \in V} \sum_{j \in V} r_i z_{ij}^t \tag{1}$$

s.t.
$$\sum_{t=1}^{T} \sum_{j \in V} z_{ij}^{t} \le 1, \quad \forall i \in V_c, i \ne j$$
 (2)

$$\sum_{t=1}^{T} \sum_{i \in V} \sum_{j \in V} (c_{ij} + e_j) z_{ij}^t \le W$$
(3)

$$\sum_{i \in V} \sum_{j \in V} (c_{ij} + e_j) z_{ij}^t \le H, \qquad \forall t \in \{1, 2, \dots, T\}$$

$$\tag{4}$$

$$\sum_{i \in V_c} z_{0i}^t = \sum_{j \in V_c} z_{j0}^t = 1, \qquad \forall t \in \{1, 2, \dots, T\}$$
 (5)

$$\sum_{i \in V} z_{ij}^t = \sum_{i \in V} z_{ji}^t, \qquad \forall i \in V, t \in \{1, 2, \dots, T\}$$
 (6)

$$2 \le u_i^t \le N, \qquad \forall i \in V_c \tag{7}$$

$$u_i^l - u_i^l + 1 \le (N - 1)(1 - z_{ij}^l). \quad \forall t \in \{1, 2, \dots, T\}, i, j \in V_c, i \ne j$$
 (8)

The objective (1) maximizes the cumulative rewards collected over T periods. Constraints (2) ensure that each node is visited at most once throughout all periods. Constraints (3) restrict the total working time across all periods to remain within the specified limit of W. Constraints (4) limit the daily working duration to remain within the threshold H. Constraints (5) guarantee that the inspection team starts and completes their tour at node 0. Furthermore, constraints (6) are formulated as flow conservation constraints. Finally, constraints (7)–(8) are employed to prevent the formation of subtours and u_i is an integer variable indicating the position of node i in the tour.

4.2. Solution approach

We employ a Lagrangian relaxation method tailored for the MPOP. The methodology begins by relaxing the constraints that couple different periods, allowing the decomposition of the MPOP into single-period subproblems that are more tractable. Subsequently, the Lagrangian dual of the relaxed problem is solved using the subgradient algorithm, which provides an upper bound for the original MPOP. Considering that the Lagrangian dual solution might not always satisfy the original constraints, we further devise an enhancement procedure to derive a feasible solution based on the Lagrangian dual solution.

4.2.1. Lagrangian relaxation

We relax constraints (2) and (3) by introducing Lagrangian multipliers $\lambda_i \ge 0$ where $i \in V_c$ and $\xi \ge 0$, respectively. Then, model (1) can be reformulated as:

$$\max_{\substack{z_{ij}^t \in \{0,1\}, u_i \in \mathbb{Z}^+ \\ s.t.}} \sum_{i \in T} \sum_{j \in V} \sum_{j \in V} r_i z_{ij}^t - \sum_{i \in V_c} \lambda_i \left(\sum_{t \in T} \sum_{j \in V} z_{ij}^t - 1 \right) - \xi \left(\sum_{t \in T} \sum_{i \in V} \sum_{j \in V} (c_{ij} + e_j) z_{ij}^t - W \right)$$

The objective of the problem above represents an upper bound (UB) on the optimal objective function value of the original problem since two constraints have been relaxed.

4.2.2. Subgradient optimization

The tightest UB could be obtained by solving the Lagrangian dual:

$$\begin{split} \min L(\lambda,\xi) &= \min \max_{z_{ij}^t \in \{0,1\}} \sum_{t \in T} \sum_{i \in V} \sum_{j \in V} \left(r_i - \lambda_i - \xi(c_{ij} + e_j) \right) z_{ij}^t + \sum_{i \in V_c} \lambda_i + \xi W \\ \text{s.t.} \quad \lambda_i &\geq 0, \quad \forall i \in V_c \\ \xi &\geq 0. \end{split}$$

We utilize a subgradient method to tackle the Lagrangian dual problem. This approach involves the iterative update of multipliers λ and ξ , contributing to the progressive enhancement of the UB over iterations. Initially set to zero, these multipliers are updated from iteration ρ to $\rho + 1$ following specific procedures:

$$\lambda_i^{\rho+1} = \max\left\{0, \ \lambda_i^{\rho} - \eta^{\rho} \left(1 - \sum_{t \in T} \sum_{i \in V} \sum_{j \in V} z_{ij}^t\right)\right\}, \qquad \forall i \in V_c$$

$$(9)$$

$$\xi^{\rho+1} = \max \left\{ 0, \, \xi^{\rho} - \eta^{\rho} \left(W - \sum_{t \in T} \sum_{i \in V} \sum_{j \in V} (c_{ij} + e_j) z_{ij}^t \right) \right\}. \tag{10}$$

The step length η^{ρ} at iteration ρ is computed as:

$$\eta^{\rho} = \frac{\beta^{\rho} \left(L(\lambda^{\rho}, \xi^{\rho}) - LB^{*} \right)}{\sqrt{\sum_{i \in V_{c}} \left(1 - \sum_{t \in T} \sum_{j \in V} z_{ij}^{t} \right)^{2} + \left(W - \sum_{t \in T} \sum_{i \in V} \sum_{j \in V} (c_{ij} + e_{j}) z_{ij}^{t} \right)^{2}}},$$

$$(11)$$

where LB* is the best found lower bound and β^{ρ} is the step length parameter.

4.2.3. Heuristic for upper bound

In each iteration of multiplier updates, we are confronted with a sequence of orienteering problems (OPs) that require solutions. As the OP is known as an NP-hard problem (Vincent et al., 2019), seeking optimal solutions can lead to significant computational expenses and may become unfeasible, particularly in the context of large-scale instances. To tackle this challenge, we strike a tradeoff between solution quality and computational burden by customizing a heuristic, offering a faster alternative for addressing the OPs

For each OP, we address it by initially solving a Traveling Salesman Problem to visit a subset of nodes. We employ a combination of the nearest insert algorithm and a 2-opt exchange procedure for this purpose, even if it may return an infeasible solution that violates the daily time constraint. The obtained solution serves as the input for the route adjustment process. In the subsequent steps, we enhance this solution through an iterative application of a drop-node and an add-node operator. In each iteration, the drop-node operator selectively eliminates the least valuable node from the route while the add-node operator includes the most valuable node from the non-visited node set. The primary aim is to uphold adherence to the daily time constraint while simultaneously minimizing the reduction in the total accumulated reward.

It should be noted that the reward distribution remains consistent across all inspection periods. As a result, solving OPs sequentially will yield an identical solution for each period. To tackle this issue, we apply an operation ensuring that previously

Algorithm 1: Heuristic to solve OPs

```
Input: Reward r_i, \forall i \in V_c, inspection time e_i, \forall i \in V_c, daily time limit H
    Output: Inspection tour set \Re for T periods
 1 Initialization: Non-visited node set V_{no} \leftarrow V_c
 2 for t = \{1, 2, ..., T\} do
          Sort V_{no} in descending order based on the reward and select the first \lceil \frac{2H}{e} \rceil nodes;
 3
          Apply the nearest neighbor algorithm and the 2-optimal exchange procedure for route generation to traverse selected nodes and obtain
 4
           a route \Re^t with travel time \Omega(\Re^t) and collected reward \Gamma(\Re^t);
          while \Omega(\Re^t) > H do
 5
 6
               Identify the node i with the least reward in \Re^t and update \Re^t \setminus \{i\};
 7
               Apply the nearest neighbor algorithm and the 2-optimal exchange procedure for route generation to traverse nodes in \Re^t;
               Update \Re^t, \Omega(\Re^t), \Gamma(\Re^t), V_{no} \leftarrow V_{no} \setminus \Re^t;
 8
          end
 q
          while \Omega(\Re^t) + e_i < H do
10
11
               Find the node
                            i^* = \arg\max\left\{\Gamma(\tilde{\mathbf{R}}^t) - \Gamma(\mathbf{R}^t)\middle|\Omega(\tilde{\mathbf{R}}^t) \leq H\right\}
                  where \tilde{\mathbf{R}}^i is the optimized route to traverse the nodes in \mathbf{R}^i with the inclusion of node i using the nearest neighbor algorithm
                 and the 2-optimal exchange procedure.
               Update \Re^t \leftarrow \tilde{\Re}^t, \Omega(\Re^t) \leftarrow \Omega(\tilde{\Re}^t), \Gamma(\Re^t) \leftarrow \Gamma(\tilde{\Re}^t), V_{no} \leftarrow V_{no} \setminus \{i^*\};
12
13
          Identify the node i with the highest reward in \Re^{t};
14
15
          Update V_{no} \leftarrow V_{no} \setminus \{i\};
16 end
```

Algorithm 2: Heuristic to find a lower bound to the original problem

```
Input: Upper bound solution \Re, inspection time e_i, \forall i \in V_i, T, total time limit W, daily time limit H, reward r_i, \forall i \in V_i
    Output: Sub-optimal solution to the original problem
 1 Initialization: prohibited list \zeta \leftarrow \emptyset, non-visited node set V_{no} \leftarrow V_c.
 2 Let \Psi(\cdot) denote an insertion algorithm and crossover and exchange improvement procedures to optimize routes with the limit of each route
      duration less than H to traverse a set of nodes.
 3 for t = \{1, 2, ..., T\} do
          S_1 = \Re^t \cap \zeta, S_2 = \Re^t - \zeta;
          \Re^t \leftarrow \Re^t \setminus S_1, \ \zeta \leftarrow \zeta \cup S_2;
 5
 6 end
 7 Run \Psi(\bigcup_{t=1}^T \Re^t) and obtain a set of routes \Phi with total travel time \Omega(\Phi) and collected reward \Gamma(\Phi);
 8 V_{no} \leftarrow V_c \setminus (\bigcup_{t=1}^T \Re^t);
 9 while \Omega(\Phi) + e_i < W do
          Find the node
10
                       i^* = \arg\max\left\{ \Gamma(\tilde{\Phi}) - \Gamma(\Phi) \middle| \Omega(\tilde{\Phi}) \le W \right\}
            where \tilde{\Phi} is a set of optimized tours returned by applying \Psi(\Phi \cup \{i\}).
          Update \Phi \leftarrow \tilde{\Phi}, \Omega(\Phi) \leftarrow \Omega(\tilde{\Phi}), \Gamma(\Phi) \leftarrow \Gamma(\tilde{\Phi}), V_{no} \leftarrow V_{no} \setminus \{i^*\};
11
12 end
```

Algorithm 3: Lagrangian heuristic

```
Input: Maximum iterations 3
    Output: z_{ij}^t, 1 - \frac{LB^*}{LB^*}
 1 Initialization:
 2 Iteration count \rho = 1;
 3 \lambda^{\rho} = 0, \xi^{\rho} = 0;
 4 Step length parameter \beta^{\rho} = 1;
 5 Solve the relaxed problem using Algorithm 1 and obtain a solution \tilde{z}_{ii}^t;
 6 Let LB = LB* = 0, UB* = L(\lambda^{\rho}, \xi^{\rho}).
    while \rho < \Im do
          Compute the step length \eta^{\rho} using (11);
 8
          Update \lambda^{\rho} and \xi^{\rho} using (9)–(10);
 9
          Solve the relaxed problems and compute L(\lambda^{\rho+1}, \xi^{\rho+1});
10
          if UB^* > L(\lambda^{\rho+1}, \xi^{\rho+1}) then
11
           UB^* \leftarrow L(\lambda^{\rho+1}, \xi^{\rho+1});
12
          end
13
          Apply Algorithm 2 with \tilde{z}_{ii}^t to obtain a feasible solution z_{ii}^t and LB;
14
          if LB* < LB then
15
16
           LB^* \leftarrow LB;
          end
17
          if UB has not decreased by more than 0.1% in past 50 iterations then
18
19
          end
20
          if (\rho \% 100) == 0 then
21
22
              Reset \beta^{\rho} to 1;
          end
23
24
          \rho = \rho + 1;
25 end
```

visited high-value nodes in the route for period t remain inaccessible in subsequent periods from t + 1 to T (see lines 14 and 15 in Algorithm 1). The detailed procedures are outlined in Algorithm 1.

4.2.4. Heuristic for lower bound

After calculating $L(\lambda, \xi)$ using the values of λ and ξ in each iteration, the next step is to obtain a feasible solution for the original problem to determine a lower bound (LB). As mentioned before, the solution \Re generated by Algorithm 1 may be infeasible since it can potentially violate the constraints (2) and (3). Therefore, it is imperative to make adjustments to \Re to ensure that the resulting solution complies with all constraints in the original problem. The step-by-step procedure for achieving this is detailed in Algorithm 2. Specifically, the output from Algorithm 1 serves as the initial solution and may involve nodes covered by routes for multiple distinct periods. The first task is to address these overlaps, guaranteeing that each node is visited only once across all periods. This task is executed through lines 3 to 6. Subsequently, the vehicle routing heuristic $\Psi(\cdot)$ is invoked in line 7 to determine routes for visiting these covered nodes while the non-visited node set is updated in line 8. Despite the total route duration being within the limit, additional valuable nodes must be identified for inclusion to increase reward collection until the maximum time duration is surpassed, as demonstrated in lines 9 to 11.

4.2.5. Lagrangian heuristic

The procedure of the proposed Lagrangian heuristic is outlined in Algorithm 3. We begin by assigning initial values to LB and Lagrangian multipliers. An iterative loop is then executed until the termination criterion is met. Within each iteration, dual steps of the subgradient optimization are carried out to enhance the UB, with concurrent updates to the feasible solution z'_{ij} . Specifically, the Lagrangian dual problem is addressed using Algorithm 1, yielding an UB. Additionally, Algorithm 2 is utilized to transform the solution of the Lagrangian dual problem into a feasible solution for the original problem.

5. Uninspected buildings damage inference

The preceding section details the approach for determining inspection routes that maximize the rewards from building damage inspection. Following this, we shift our focus to applying the collected damage data to train a GPR model for estimating damage in uninspected buildings. To ensure clarity, we begin with an overview of GPR and its common applications, then proceed to discuss the critical configurations, with a particular emphasis on the selection of kernel functions and the key hyperparameters that have demonstrated best performance in our experiments.

5.1. Gaussian process regression

GPR stands as a robust non-parametric Bayesian approach, particularly suited for regression tasks where the relationship between input variables and outputs is complex (Schulz et al., 2018). Distinct from conventional machine learning algorithms that predict a single value, GPR provides a predictive output distribution for a given input. Fundamentally, GPR employs the sampling of multivariate Gaussian functions to best fit the given inputs, with the kernel function measuring the similarity between input pairs. The effectiveness of GPR relies on the hyperparameters of the chosen kernel function, which require careful selection and optimization. The typical workflow for GPR involves gathering input—output data, choosing an appropriate kernel function for the problem at hand, optimizing the hyperparameters of the determined kernel function, and deploying the trained GPR model for predictions.

GPR's versatility is evidenced by its widespread application across diverse fields. In the manufacturing sector, it has been utilized for evaluating tool wear status (Kong et al., 2018) and predicting the capacity of lithium-ion batteries (Liu et al., 2019). In water resource management, GPR aids in forecasting monthly streamflows (Sun et al., 2014) and predicting water temperatures (Grbić et al., 2013). Beyond these, GPR's utility extends to estimating building energy consumption (Zeng et al., 2020) and projecting mortality rates (Wu and Wang, 2018), demonstrating its broad applicability and effectiveness.

5.2. Post-earthquake building damage inference

In this study, we utilize GPR to deduce earthquake-induced damage in buildings. This approach is supported by previous research, such as the work by Sheibani and Ou (2021), Sheibani et al. (2022), and Cheraghi et al. (2024), demonstrating the reliability of GPR models in damage estimation. Our discussion starts by outlining the mathematical framework underpinning GPR as follows. The function f serves as our predictive tool, capturing incurred building damage. This function links a vector \mathbf{x} , encompassing a set of structural and locational attributes of a building (see Table 1), to quantifiable damage metric $f(\mathbf{x})$. Recognizing the inherent uncertainties of earthquake damage, we propose that the true function $f(\cdot)$ can be represented as a Gaussian process (GP), a framework that conceives a set of observations as manifestations of a multivariate Gaussian distribution (Williams and Rasmussen, 2006). The GP is specified by its mean function $f(\cdot)$ and covariance function $f(\cdot)$:

$$f(\mathbf{x}) \sim \mathcal{GP}(m(\mathbf{x}), \mathcal{D}(\mathbf{x}, \mathbf{x}')),$$

where

$$m(\mathbf{x}) = \mathbb{E}[f(\mathbf{x})],$$

$$\wp(\mathbf{x}, \mathbf{x}') = \mathbb{E}[(f(\mathbf{x}) - m(\mathbf{x}))(f(\mathbf{x}') - m(\mathbf{x}'))].$$

Given the typical scarcity or uncertainty of damage data, a zero-mean prior, $m(\cdot) = 0$, is often assumed (Sheibani and Ou, 2021). On-site inspections often come with noise, stemming from factors like accessibility issues or subjective evaluations. As such, the estimates provided by inspection teams are perceived as noisy approximations of true damages. Expressing these estimates as y, they relate to the underlying damage function f as:

$$y = f(\mathbf{x}) + \epsilon, \tag{12}$$

with ϵ being a zero-mean Gaussian noise term characterized by variance σ_n^2 .

With our training data, or inspection records, represented as (X, y), and potential test locations as X', our objective becomes inferring the probable damage values at X', denoted by $\hat{\mathbf{f}}$. This inference follows the distribution:

$$\hat{\mathbf{f}}|X, \mathbf{y}, X' \sim \mathcal{N}(\hat{\boldsymbol{\mu}}, \hat{\boldsymbol{\Sigma}}),$$

where

$$\hat{\boldsymbol{\mu}} = K_{X'X}[K_{XX} + \sigma_n^2 I]^{-1} \mathbf{y},$$

$$\hat{\boldsymbol{\Sigma}} = K_{X'X'} - K_{X'X}[K_{XX} + \sigma_n^2 I]^{-1} K_{XX'}.$$
(13)

Here, K_{ij} stands for a covariance matrix, its entries derived from our chosen kernel function evaluated at different data points.

5.3. Kernel function and hyperparameter tuning

The kernel function (or covariance function) \mathscr{D} is a central aspect of GPR. This function captures how correlated two data points \mathbf{x}_i and \mathbf{x}_j are in our model. Specifically, for any two data points \mathbf{x}_i and \mathbf{x}_j , $\mathscr{D}(\mathbf{x}_i, \mathbf{x}_j)$ denotes the covariance between the function values, $\text{cov}[f(\mathbf{x}_i), f(\mathbf{x}_i)]$.

Selecting the right kernel function is an important step in building the damage inference model as it encodes the prior belief about the unknown function f (Williams and Rasmussen, 2006). Sheibani and Ou (2021) compare various kernel functions to predict regional earthquake damage. Their findings suggest that the rational quadratic (RQ) kernel, when combined with the Automatic Relevance Determination (ARD) feature, accurately captures patterns across different dimensions, leading to better predictive performance. ARD kernels help the model highlight the most important features of the data while downplaying less significant ones. After training, the effectiveness of each feature in our model can be inferred from its corresponding length scale.

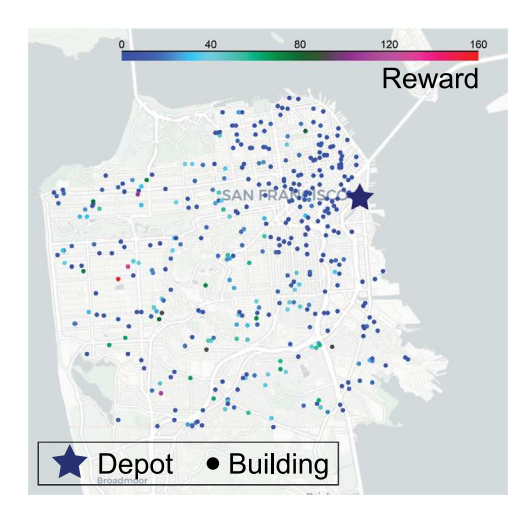


Fig. 4. The spatial distribution and associated reward of buildings in a single instance.

The RQ kernel is described as:

$$\wp_{RQ}(\mathbf{x}_i, \mathbf{x}_j) = \sigma_f^2 \left[1 + (\mathbf{x}_i - \mathbf{x}_j)^{\mathsf{T}} \frac{\mathbf{M}}{2\alpha} (\mathbf{x}_i - \mathbf{x}_j) \right]^{-\alpha},$$

where σ_f^2 is the signal variance, **M** is a diagonal matrix holding the length scales tied to each feature, and α is a parameter that modifies how heavily these lengthscales influence the kernel.

Posterior covariance depends on both the chosen kernel and the noise variance σ_n^2 . The entire model is defined by a group of hyperparameters, labeled θ . These hyperparameters consist of the signal variance, length scales, α , and the noise variance. To train the model and identify the best hyperparameters, we maximize the marginal likelihood of observations for the hyperparameters:

$$\theta^* = \underset{\theta}{\operatorname{argmax}} \log p(\mathbf{y}|X, \theta),$$

where θ^* denotes the optimal values of hyperparameters.

Finally, the log marginal likelihood of our noisy observations, given a set of hyperparameters θ , is found by:

$$\log p(\mathbf{y}|X,\boldsymbol{\theta}) = -\frac{1}{2}\mathbf{y}^{\top} \left(K_{XX} + \sigma_n^2 I\right)^{-1} \mathbf{y} - \frac{1}{2} \left|K_{XX} + \sigma_n^2 I\right| - \frac{n}{2} \log(2\pi),$$

where n represents the size of a training dataset.

6. Numerical experiments

In this section, we validate the performance of the proposed Lagrangian heuristic in optimizing multi-period inspection routes. As examined in the six small instances, the proposed heuristic offers optimal solutions that achieve objectives identical to those generated by mathematical programming software, providing us with a solid foundation for its application to more substantial datasets. A detailed examination of this evaluation is deferred to Appendix B. Following this, we proceed to apply the developed framework to large instances utilizing real-world data from San Francisco. These instances serve as the testing ground for evaluating the efficacy of our novel approach to building damage assessment. To emphasize the advantages of multi-period planning over the period-by-period planning approach, we have also applied the period-by-period planning technique in these scenarios to conduct a comparative analysis.

6.1. Inspection experimental setup

To conduct a thorough examination of the framework, we perform 20 random selections, each using 80% of the data from S, generating 20 unique datasets (S_{80}). Within each S_{80} instance, a clustering-based sampling technique is employed to identify representative buildings for inspection and subsequent model training for damage inference.

For each of the 20 randomly selected subsets of data, the k-means++ clustering algorithm is applied and results in a total of $|V_c| = 500$ buildings selected for inspection. The spatial distribution and reward assignment for the representative buildings in a single instance is shown in Fig. 4. The inspection horizon is set at T = 10 periods, and each period has a regular working time of 8 h and a maximum working duration H of 10 h, inclusive of travel time and a 30-min inspection time per building. The selection of a 30-min inspection time aligns with operational norms for "rapid evaluations" as recommended in Applied Technology Council (ATC) Field Manual (ATC, 2005) and Federal Emergency Management Agency (FEMA) Post-disaster Building Safety Evaluation

Table 2			
Reward collection via period-by-period	planning and	multi-period	planning.

Instance	Multi-period		Period-by-period		Imp.
No.	Reward	# Inspections	Reward	# Inspections	(%)
1	5866	172	5599	149	4.77
2	6085	179	5780	152	5.28
3	5698	177	5426	153	5.01
4	5954	176	5678	151	4.86
5	5975	179	5696	154	4.90
6	5731	173	5470	149	4.77
7	5703	174	5465	152	4.35
8	6014	176	5759	154	4.43
9	5934	177	5676	152	4.55
10	6096	176	5831	151	4.54
11	5965	178	5718	155	4.32
12	6017	177	5757	154	4.52
13	6026	176	5777	152	4.31
14	5827	177	5574	154	4.54
15	6053	178	5782	153	4.69
16	5796	179	5539	153	4.64
17	5992	177	5738	154	4.43
18	6014	177	5761	153	4.39
19	5717	178	5481	155	4.31
20	6031	178	5758	153	4.74

Guidance (FEMA, 2019). The cumulative working duration W across all periods is set to 80 h. The travel time c_{ij} between buildings i and j is calculated by dividing the Euclidean distance between the two buildings by a constant speed of 15 kilometers per hour.

The study encompasses a detailed analysis of 20 large-scale instances, each featuring 500 buildings, with data extracted from the San Francisco testbed. For the multi-period inspection routing, the termination criterion of the proposed Lagrangian heuristic is established at a limit of 300 iterations for all instances. We execute the proposed heuristics and showcase the optimality gaps related to the best solution to the Lagrangian dual, as denoted by $\frac{UB - LB}{UB} \times 100\%$.

6.2. Evaluation criteria for damage inference

In our numerical experiments, we employ three error metrics to measure the predictive performance of the GPR model, including the standard mean squared error (SMSE), the mean absolute logarithmic error (MALE), and the mean absolute percentage error (MAPE). For n test data points in S', with predictions \hat{y} and ground truth values y, the error measures are defined as:

$$\begin{aligned} \text{SMSE} &= \frac{1}{n} \frac{\sum_{i=1}^{n} (\hat{y}_i - y_i)^2}{\text{Var}(\mathbf{y})}, \\ \text{MALE} &= \frac{1}{n} \sum_{i=1}^{n} \left| \log \frac{\hat{y}_i}{y_i} \right|, \\ \text{MAPE} &= \frac{1}{n} \sum_{i=1}^{n} \left| \frac{\hat{y}_i - y_i}{y_i} \right| \times 100\%, \end{aligned}$$

where \hat{y} is the predictive mean of the GP, as defined in (13).

In addition to the error metrics used to measure the overall performance of the GPR model, we evaluate the percentage of accurate predictions by considering the relative difference (RD) between predicted values and the ground truth,

$$RD = \left| \frac{\hat{\mathbf{y}} - \mathbf{y}}{\mathbf{y}} \right|,$$

where \hat{y} represents the vector of predicted values while y corresponds to the vector of ground truth values. The percentage of testing data points for which RD is less than 0.2 (i.e., RD < 0.2) serves as a metric to quantify the precision of predictions.

6.3. Experimental results

Table 2 displays the total collected rewards achieved through both period-by-period and multi-period planning across 10 periods for the set of 20 instances. The multi-period planning approach consistently outperforms the period-by-period planning strategy, showcasing an average improvement of 4.62%, accompanied by a modest standard deviation of 0.26%, across all twenty instances. It is noteworthy that the proposed algorithm exhibits impressive computational efficiency and converges rapidly. As demonstrated in Fig. 5, it reveals a clear and absolute convergence between LB and UB across the six presented instances. Notably, when a robust LB is established, the UB rapidly converges toward the best-found LB.

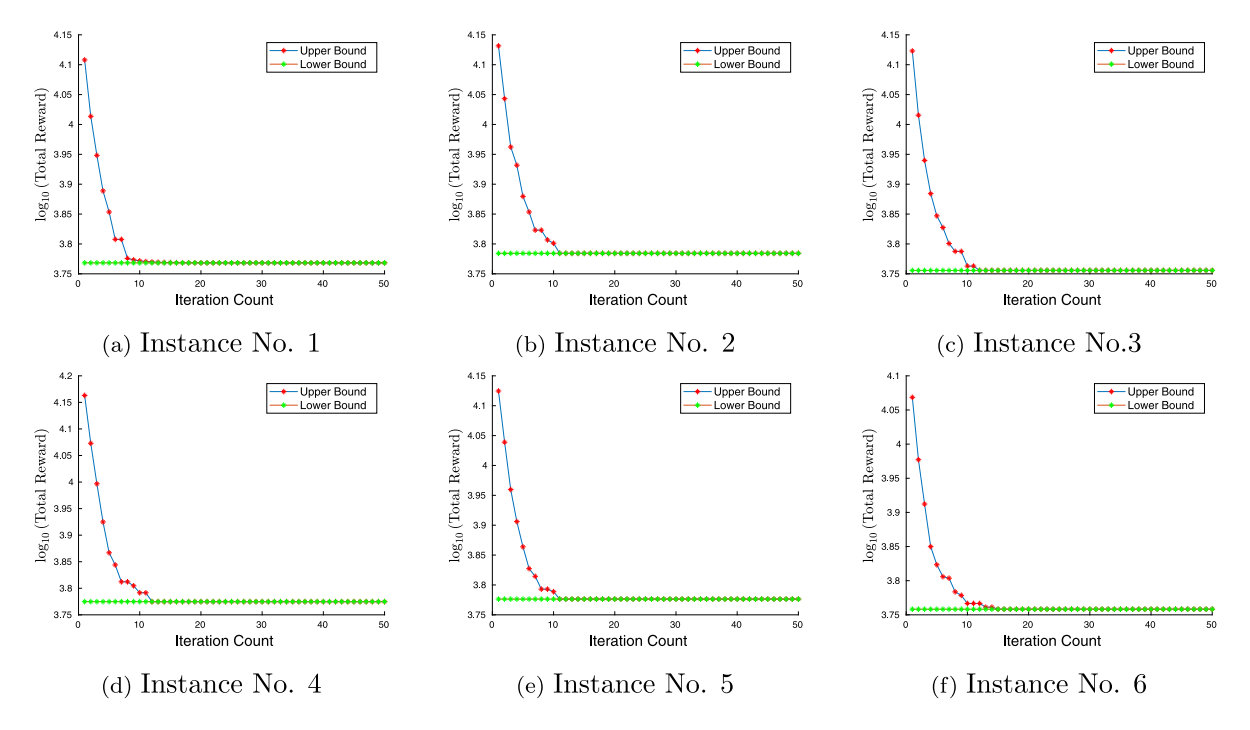


Fig. 5. The gaps between the lower bound and upper bound in the six large-size instances.

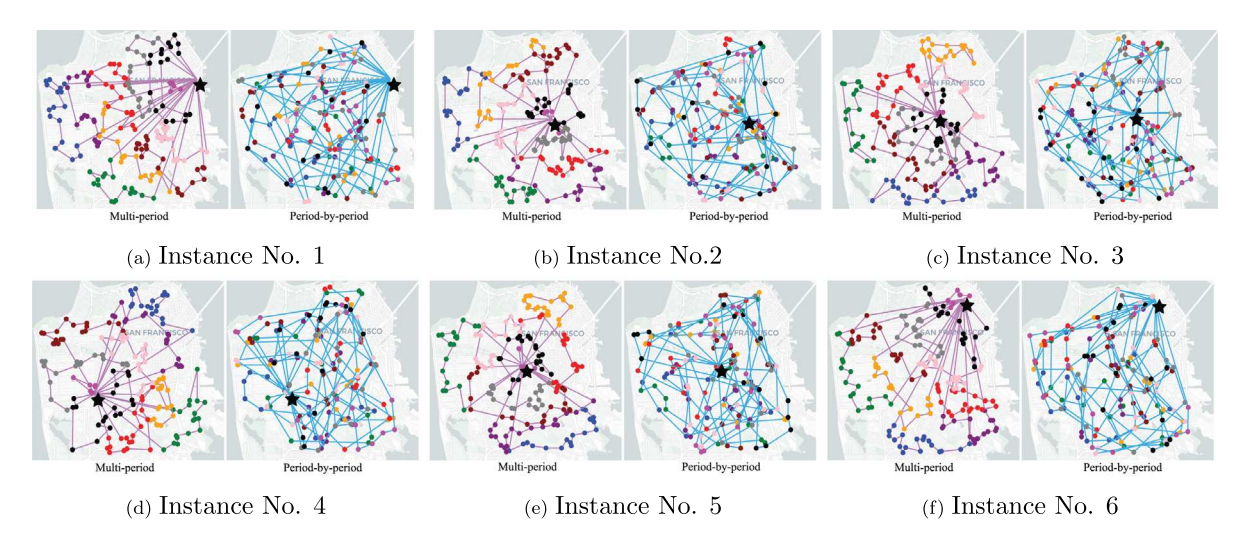


Fig. 6. Inspection routes under multi-period and period-by-period planning for the six large-size instances.

Fig. 6 illustrates the inspection routes generated by both multi-period planning and period-by-period planning strategies. The routes generated by the former strategy exhibit a higher level of organization, whereas the routes derived from period-by-period planning appear considerably more chaotic. This discrepancy arises from the fact that multi-period planning devises routes from a holistic viewpoint, while period-by-period planning prioritizes maximizing reward collection for individual periods in a myopic manner.

The cumulative reward gained from implementing two sets of inspection routes over a 10-period span is presented in Fig. 7. It indicates that the strategy of designing inspection routes on a period-by-period basis effectively prioritizes the inspection of high-value buildings during each period. As a result, in the early stages, this approach facilitates the collection of a significantly greater amount of reward. However, in the final two or three periods, due to the considerable time spent reaching high-value buildings located far from the depot, the ability to inspect additional nodes and attain higher rewards diminishes. In contrast, the multi-period planning approach employs a more holistic route design, ensuring a consistent rate of reward acquisition throughout all periods.

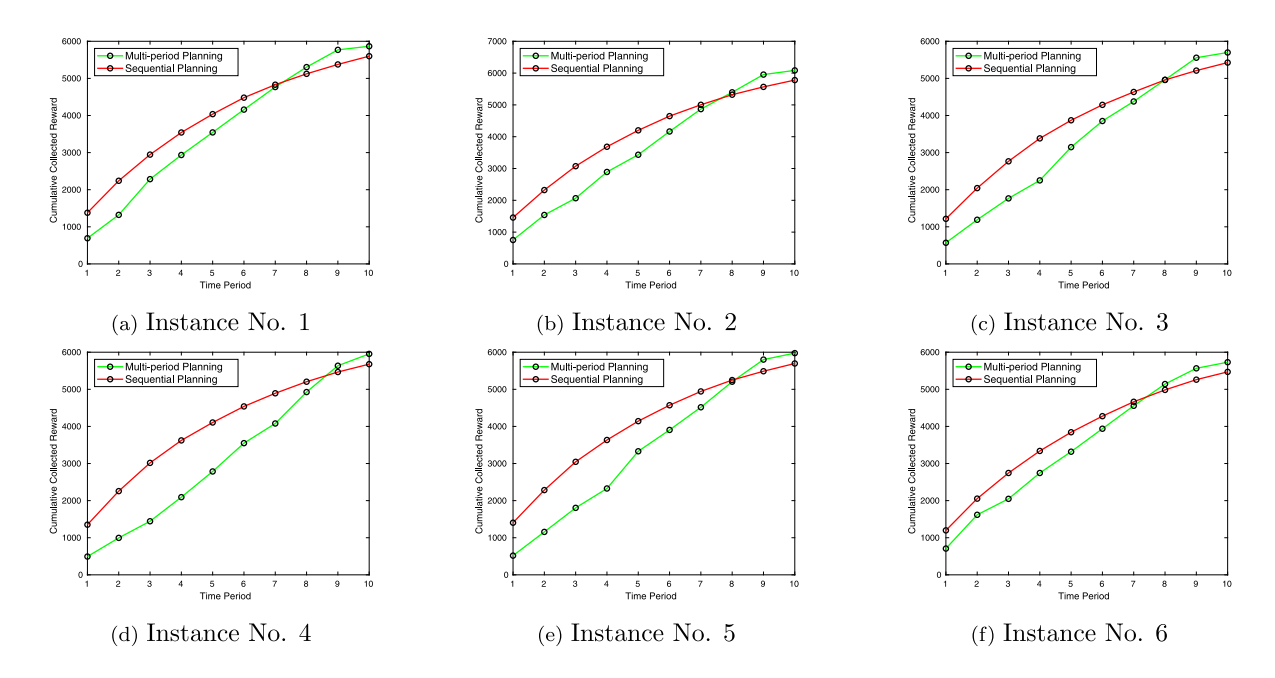


Fig. 7. Cumulative reward collection across 10 periods under period-by-period and multi-period planning for the six large-size instances.

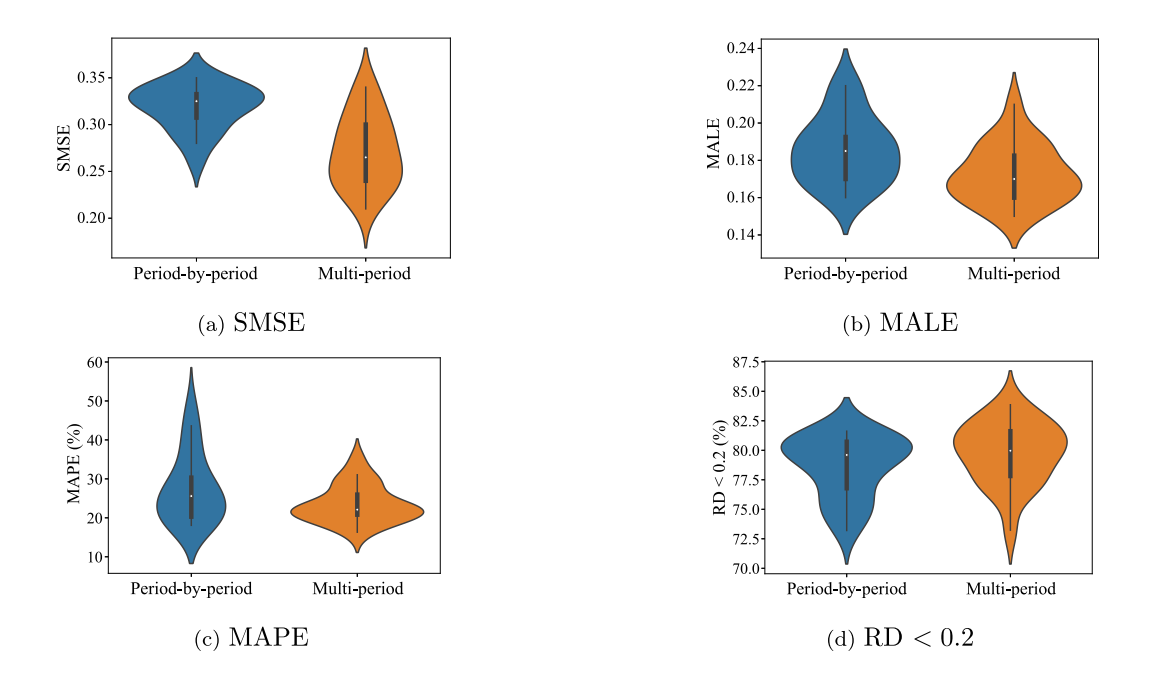
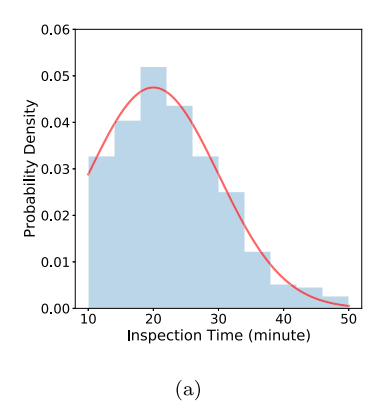
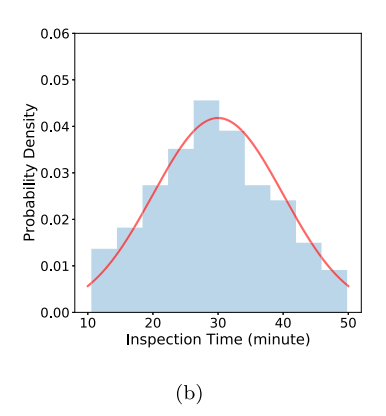


Fig. 8. Accuracy comparison of the GPR model trained with buildings damage data collected under period-by-period and multi-period planning, measured by SMSE, MALE, MAPE, and RD < 0.2.

Ultimately, our multi-period routing approach leads to higher rewards by inspecting more buildings as the timeframe draws to a close.

Using damage data collected with two distinct inspection strategies, we train separate GPR models and conduct a comparative assessment of their estimation accuracy, as measured by SMSE, MALE, MAPE, and RD < 0.2. Fig. 8 illustrates the estimation accuracy distribution of these two GPR models across 20 test datasets. The GPR model trained using the multi-period approach outperforms the model trained with the period-by-period one. To quantify this improvement, we computed the average enhancements across





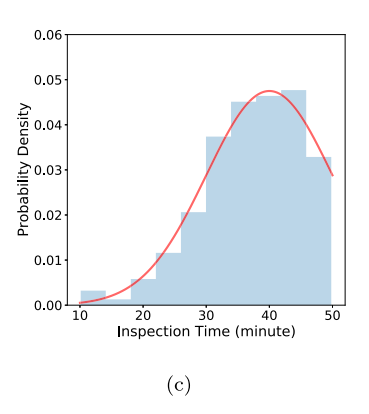


Fig. 9. The inspection times are generated randomly from truncated normal distributions. The mean values for these distributions are: (a) 20 min, (b) 30 min, and (c) 40 min. The standard deviation remains fixed at 10 min for all cases.

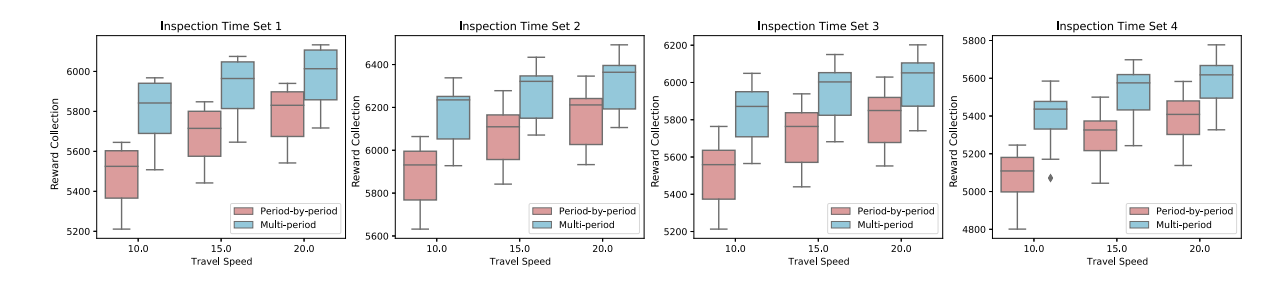


Fig. 10. The cumulative reward collection over all periods via period-by-period and multi-period routing strategy. The inspection time sets 1, 2, 3, and 4 correspond to inspection times generated from the uniform and truncated normal distributions with three different mean values, respectively.

the test datasets, resulting in improvements of 14.75% for SMSE, 7.01% for MALE, 14.67% for MAPE, and 1.41% for RD < 0.2, respectively.

In our study, we address a deterministic multi-period routing problem with fixed travel speed and inspection time for each building. Recognizing the need to test the model's robustness against real-world variations, we conduct a sensitivity analysis on travel speed and inspection time per building. The analysis involves three travel speeds (10 km/h, 15 km/h, and 20 km/h) and four sets of inspection times. These times are generated from uniform and truncated normal distributions with mean values set at 20 min, 30 min, and 40 min, each with a constant standard deviation of 10 min. Inspection times are constrained within the interval of 10 to 50 min to ensure validity. The distributions of inspection times generated from the truncated normal distributions are illustrated in Fig. 9.

We apply the proposed approach for inspection routing and building damage estimation across each combination of travel speeds and inspection time sets, considering 20 large-size instances with 10 periods. The accumulated rewards obtained from inspection routes determined using period-by-period and multi-period routing strategies are depicted in Fig. 10. A notable observation is that the cumulative reward collected through multi-period routing consistently surpasses that collected via period-by-period routing. Moreover, it can be observed that the inspection times with a smaller mean value and a faster travel speed result in greater reward collection. This is because less time is spent on inspection and travel between buildings, enabling more buildings to be inspected, which aligns with practical considerations.

The accuracy distribution of the trained GPR models over 20 test datasets, measured with SMSE, MALE, MAPE, and RD < 0.2, are depicted in Fig. 11. We can find that the accuracy of building damage inference based on obtained damage data collected via the multi-period routing strategy is more robust compared to the period-by-period routing strategy. Additionally, we understand that the accuracy of the GPR model heavily relies on the quantity of reward collected. As demonstrated in Fig. 10, faster travel speeds and shorter inspection times correlate with increased reward collection. Therefore, the setting of faster travel speeds and shorter inspection times leads to more accurate damage estimation, which aligns with the trend presented in Fig. 11.

7. Conclusion

This work introduces a new framework, blending the MPOP with a GPR model for effective building damage assessment following an earthquake. This unique combination not only improves the assessment of earthquake-induced building damage but also tackles

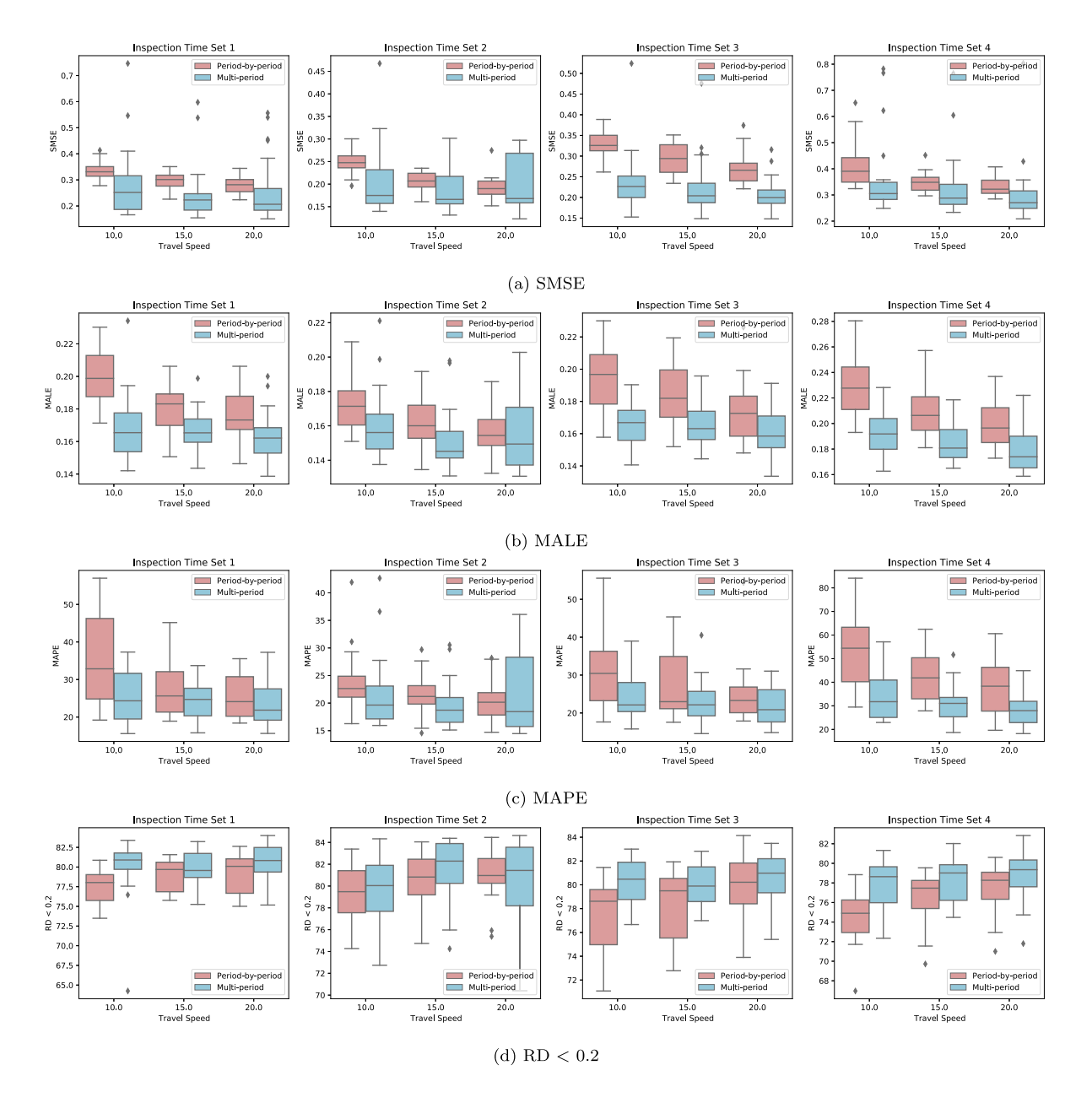


Fig. 11. The accuracy of the GPR models trained using building damage data collected under period-by-period and multi-period planning is compared across different combinations of travel speeds and inspection time setups. The evaluation metrics used include the SMSE, MALE, MAPE, and RD < 0.2.

the issues inherent to traditional inspection routes designed period by period. For handling large-scale inspection routing scenarios, we develop a Lagrangian relaxation method paired with tailored heuristics.

Our proposed approach is validated through simulation data sourced from the San Francisco Bay Area. The integration of a specialized inspection reward within the MPOP framework has yielded substantial enhancements in both damage data collection and the accuracy of the GPR model in damage estimation. These improvements are consistently observed across all four evaluation metrics, underscoring a significant advantage compared to the conventional period-by-period inspection routing strategy.

Essentially, this methodology offers a more comprehensive understanding of building damage, allowing more accurate damage predictions. This improved knowledge is crucial for decision-makers, aiding them in formulating more effective and prioritized recovery strategies and ensuring optimal resource allocation.

Looking ahead, there are several exciting possibilities for further research. One significant improvement could involve the use of an active learning approach. In this method, the rewards would be adjusted after each period's inspections, allowing the system's

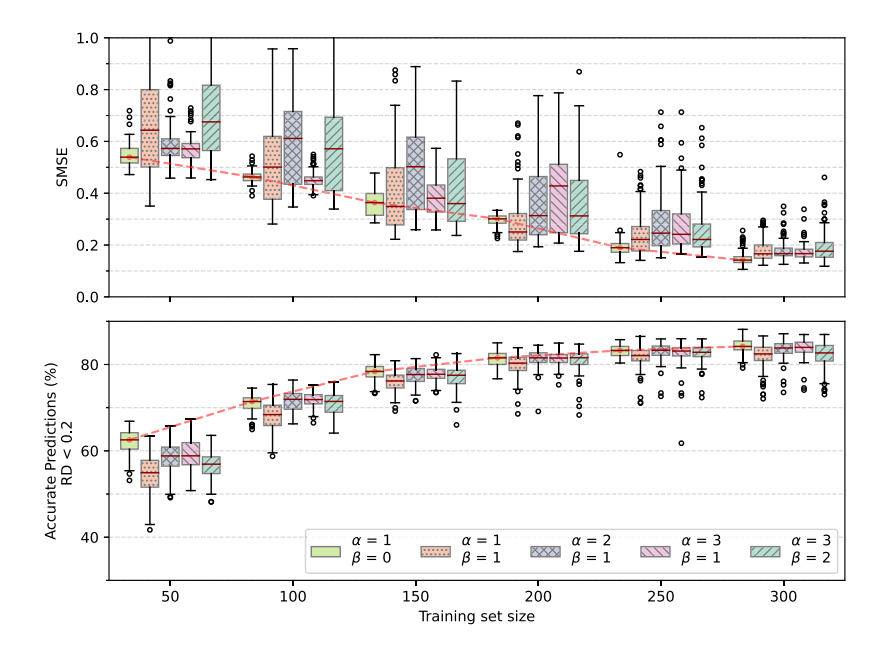


Fig. 12. Percentage of accurate predictions across various training set sizes and reward criteria.

predictions and decisions to continuously improve and align with the most recent damage data and observations. Additionally, adding a rolling horizon strategy for multi-period inspection planning would ensure that the model remains flexible. It would adapt to changing situations by adjusting routes based on the latest available data. This ongoing feedback loop would further increase the accuracy and efficiency of our framework.

CRediT authorship contribution statement

Yinhu Wang: Writing – original draft, Review & editing, Visualization, Methodology, Formal analysis. Amirhossein Cheraghi: Writing – original draft, Review & editing, Visualization, Methodology, Formal analysis. Ge Ou: Writing – review & editing, Supervision, Funding acquisition, Conceptualization. Nikola Marković: Writing – review & editing, Supervision, Funding acquisition, Conceptualization.

Declaration of competing interest

The authors declare that they have no known competing financial interests or personal relationships that could have appeared to influence the work reported in this paper.

Declaration of Generative AI and AI-assisted technologies in the writing process

During the preparation of this work the authors used ChatGPT 3.5 in order to enhance both readability and language proficiency as well as the generation of Fig. 1(b). After using this tool, the authors reviewed and edited the content as needed and took full responsibility for the content of the publication.

Acknowledgments

This work was funded by the National Science Foundation, United States grant 2112758. This support is gratefully acknowledged, but it implies no endorsement of the findings.

Appendix A. Further exploration of inspection reward

In our framework, we employ a clustering approach to identify representative buildings and link inspection rewards to each of these selected representatives. As outlined in Section 3.3, the reward is determined based on the size of the cluster. Notably, this simple method works better than other more complex strategies.

 $0 \rightarrow 18 \rightarrow 12 \rightarrow 11 \rightarrow 0$

Instance No.	Lagrangian heuristic		Mathematical programming solver		
	Total reward	Inspection routes	Total reward	Inspection routes	
1	207	$0 \rightarrow 11 \rightarrow 10 \rightarrow 17 \rightarrow 9 \rightarrow 13 \rightarrow 0$ $0 \rightarrow 15 \rightarrow 14 \rightarrow 0$	207	$0 \rightarrow 11 \rightarrow 10 \rightarrow 17 \rightarrow 9 \rightarrow 13 \rightarrow 0$ $0 \rightarrow 14 \rightarrow 15 \rightarrow 0$	
2	582	$0 \rightarrow 18 \rightarrow 16 \rightarrow 13 \rightarrow 14 \rightarrow 0$ $0 \rightarrow 5 \rightarrow 17 \rightarrow 12 \rightarrow 0$	582	$0 \rightarrow 18 \rightarrow 16 \rightarrow 13 \rightarrow 14 \rightarrow 0$ $0 \rightarrow 5 \rightarrow 17 \rightarrow 12 \rightarrow 0$	
3	412	$0 \rightarrow 18 \rightarrow 5 \rightarrow 14 \rightarrow 17 \rightarrow 2 \rightarrow 0$ $0 \rightarrow 9 \rightarrow 13 \rightarrow 16 \rightarrow 0$	412	$0 \rightarrow 2 \rightarrow 17 \rightarrow 14 \rightarrow 5 \rightarrow 18 \rightarrow 0$ $0 \rightarrow 9 \rightarrow 13 \rightarrow 16 \rightarrow 0$	
4	528	$0 \rightarrow 9 \rightarrow 2 \rightarrow 20 \rightarrow 12 \rightarrow 0$ $0 \rightarrow 17 \rightarrow 8 \rightarrow 18 \rightarrow 0$	528	$0 \rightarrow 20 \rightarrow 12 \rightarrow 18 \rightarrow 8 \rightarrow 0$ $0 \rightarrow 2 \rightarrow 9 \rightarrow 17 \rightarrow 0$	
5	410	$0 \rightarrow 17 \rightarrow 2 \rightarrow 5 \rightarrow 3 \rightarrow 20 \rightarrow 0$ $0 \rightarrow 19 \rightarrow 7 \rightarrow 16 \rightarrow 0$	410	$0 \rightarrow 20 \rightarrow 3 \rightarrow 5 \rightarrow 2 \rightarrow 17 \rightarrow 0$ $0 \rightarrow 16 \rightarrow 7 \rightarrow 19 \rightarrow 0$	
6	466	$0 \rightarrow 4 \rightarrow 20 \rightarrow 15 \rightarrow 12 \rightarrow 0$	466	$0 \rightarrow 20 \rightarrow 15 \rightarrow 4 \rightarrow 0$	

Table 3
Inspection routes and reward collection generated with mathematical programming solver and Lagrangian heuristic for six small-size instances

One such strategy involves using "inertia", a measure of within-cluster variance, to refine the reward assignment. The core of the idea is that clusters with lower inertia have more similar data points, and their candidate samples could better represent data within those clusters for predictive modeling. We test the combination of cluster size and inertia for reward assignment.

 $0 \rightarrow 18 \rightarrow 11 \rightarrow 0$

Recalling that C_i represents the *i*th cluster and μ_i its centroid, we consider a reward based on the ratio of cluster size to its inertia. This approach is grounded in the hypothesis that clusters with a greater number of data points and lower variance are potentially more valuable. Defined as:

$$r_i = \frac{\left|\mathcal{C}_i\right|^{\alpha}}{\left[\sum_{x_i \in \mathcal{C}_i} (x_j - \mu_i)^2\right]^{\beta}},$$

the reward r_i for the *i*th cluster is regulated by the parameters α and β , which are introduced to adjust the relative impact of each factor.

Using features from Table 1, we group the dataset into 500 clusters. Buildings closest to the centroids of these clusters are chosen as potential inspection candidates. We then train the GPR model with data points prioritized by different α and β combinations.

Fig. 12 illustrates the performance of the GPR model under various reward assignment strategies. The results come from 100 tests to minimize biases from randomness in the clustering and dataset selection. In the top part of the figure, the y-axis shows SMSE, while the bottom shows the percentage of accurate predictions (i.e., data points with RD < 0.2).

The GPR model improves with more training data. Focusing on cluster size, setting $\alpha = 1$ and $\beta = 0$, consistently yields the best results, leading to lower SMSE values and higher RD. Including inertia in our reward calculations does not give significant benefits compared to only considering cluster size. This finding further backs our choice to prioritize cluster size as the primary factor for the inspection reward.

Appendix B. Evaluation of the Lagrangian heuristic

In the main body of the manuscript, our proposed Lagrangian heuristic framework is primarily applied to large-scale instances, showcasing its scalability and practical utility. However, to assess the accuracy and efficiency of the heuristic, it is paramount to compare its performance against optimal solutions. Therefore, in this section, we evaluate the heuristic on small instances where exact solutions can be obtained through mathematical programming software.

For each of the six randomly generated small instances, a total of $|V_c| = 20$ buildings are included as representative buildings. The inspection horizon is fixed at T = 2 periods, with each period allowing a maximum working duration of 2.5 h, inclusive of travel and a 0.25-h inspection time per building. The total working time across two periods is 4 h. Travel times c_{ij} between any two buildings i and j, are computed using Euclidean distances and an assumed constant speed of 15 kilometers per hour.

Table 3 illustrates the inspection routes and corresponding total rewards gained across two periods. Our proposed heuristic returns the optimal solution for these six small instances while there are some minor variations in inspection routes in comparison to the routes generated by the mathematical programming software. The visual representation of two sets of inspection routes for each small instance can be observed in Fig. 13. Each subfigure features a side-by-side comparison. The left panel displays the inspection routes generated by the mathematical programming software, while the right panel showcases the inspection routes determined by our proposed heuristic.

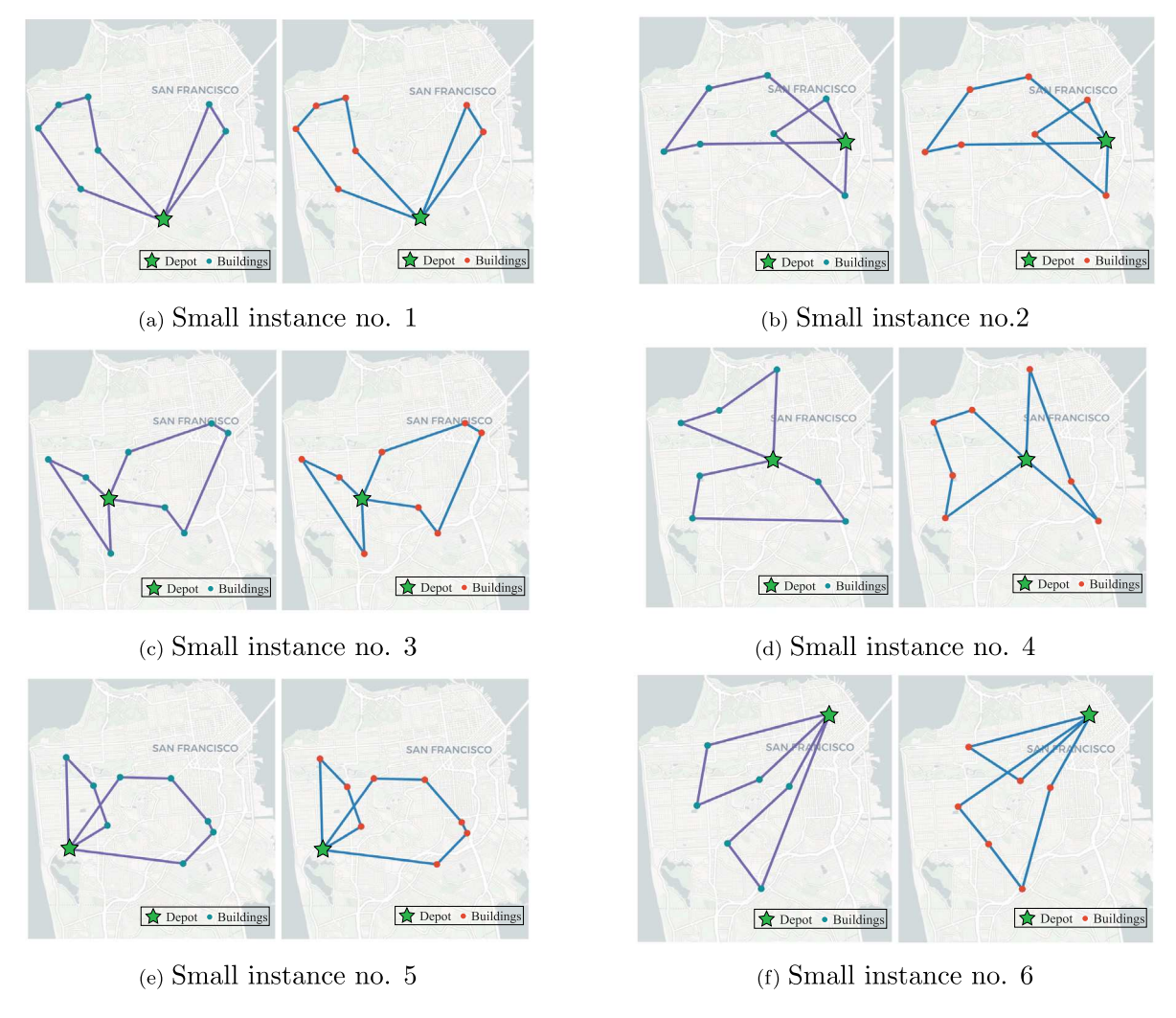


Fig. 13. Inspection routes generated with mathematical programming software and Lagrangian heuristic for six small instances.

References

Arias, A., 1970. A Measure of Earthquake Intensity: Seismic Design for Nuclear Power Plants. Massachusetts Institute of Technology.

Arthur, D., Vassilvitskii, S., 2006. K-means++: The Advantages of Careful Seeding. Technical Report, Stanford.

ATC, 2005. Field Manual: Procedures for Postearthquake Safety Evaluation of Buildings, ATC-20-1 Report, second ed. Applied Technology Council, Redwood City, California.

Bodenmann, L., Reuland, Y., Stojadinović, B., 2023. Dynamic post-earthquake updating of regional damage estimates using Gaussian Processes. Reliab. Eng. Syst. Saf. 109201.

Cha, Y.-J., Choi, W., Suh, G., Mahmoudkhani, S., Büyüköztürk, O., 2018. Autonomous structural visual inspection using region-based deep learning for detecting multiple damage types. Comput.-Aided Civ. Infrastruct. Eng. 33 (9), 731–747.

Chen, F., Yu, B., 2019. Earthquake-induced building damage mapping based on multi-task deep learning framework. IEEE Access 7, 181396-181404.

Cheraghi, A., Wang, Y., Marković, N., Ou, G., 2024. Efficient post-earthquake reconnaissance planning using adaptive batch-mode active learning. Adv. Eng. Inform. 60, 102414.

Coulston, J.W., Blinn, C.E., Thomas, V.A., Wynne, R.H., 2016. Approximating prediction uncertainty for random forest regression models. Photogramm. Eng. Remote Sens. 82 (3), 189–197.

Cui, L., Jing, X., Wang, Y., Huan, Y., Xu, Y., Zhang, Q., 2022. Improved swin transformer-based semantic segmentation of postearthquake dense buildings in urban areas using remote sensing images. IEEE J. Sel. Top. Appl. Earth Obs. Remote Sens. 16, 369–385.

Dayarian, I., Crainic, T.G., Gendreau, M., Rei, W., 2016. An adaptive large-neighborhood search heuristic for a multi-period vehicle routing problem. Transp. Res. E 95, 95–123.

de Castro Pena, G., Santos, A.C., Prins, C., 2023. Solving the integrated multi-period scheduling routing problem for cleaning debris in the aftermath of disasters. European J. Oper. Res. 306 (1), 156–172.

Demir, B., Persello, C., Bruzzone, L., 2010. Batch-mode active-learning methods for the interactive classification of remote sensing images. IEEE Trans. Geosci. Remote Sens. 49 (3), 1014–1031.

- Didier, M., Baumberger, S., Tobler, R., Esposito, S., Ghosh, S., Stojadinovic, B., 2017. Improving post-earthquake building safety evaluation using the 2015 Gorkha, Nepal, Earthquake Rapid Visual Damage Assessment Data. Earthq. Spectra 33 (1_suppl), 415–438.
- Dong, L., Shan, J., 2013. A comprehensive review of earthquake-induced building damage detection with remote sensing techniques. ISPRS J. Photogramm. Remote Sens. 84, 85–99.
- Elhaddad, W., McKenna, F., Rynge, M., Lowe, J., Wang, C., Zsarnoczay, A., 2019. NHERI-SimCenter/WorkflowRegionalEarthquake: rWHALE (Version v1. 1.0). Zenodo.
- Ezugwu, A.E.-S., Agbaje, M.B., Aljojo, N., Els, R., Chiroma, H., Abd Elaziz, M., 2020. A comparative performance study of hybrid firefly algorithms for automatic data clustering. IEEE Access 8, 121089–121118.
- Fajfar, P., Vidic, T., Fischinger, M., 1990. A measure of earthquake motion capacity to damage medium-period structures. Soil Dyn. Earthq. Eng. 9 (5), 236–242. Farooqui, M., Quadri, S.A., Suriya, S.S., Khan, M.A., Ovais, M., Sohail, Z., Shoaib, S., Tohid, H., Hassan, M., 2017. Posttraumatic stress disorder: A serious post-earthquake complication. Trends Psychiatry Psychother. 39, 135–143.
- FEMA, 2019. Post-disaster building safety evaluation guidance (FEMA P-2055).
- Franke, K.W., Lingwall, B.N., Zimmaro, P., Kayen, R.E., Tommasi, P., Chiabrando, F., Santo, A., 2018. Phased reconnaissance approach to documenting landslides following the 2016 Central Italy Earthquakes. Earthq. Spectra 34 (4), 1693–1719.
- Frolova, N., Larionov, V., Bonnin, J., Sushchev, S., Ugarov, A., Kozlov, M., 2017. Loss caused by earthquakes: Rapid estimates. Nat. Hazards 88, 63-80.
- Ghimire, S., Guéguen, P., Giffard-Roisin, S., Schorlemmer, D., 2022. Testing machine learning models for seismic damage prediction at a regional scale using building-damage dataset compiled after the 2015 Gorkha Nepal earthquake. Earthq. Spectra 38 (4), 2970–2993.
- Grbić, R., Kurtagić, D., Slišković, D., 2013. Stream water temperature prediction based on Gaussian process regression. Expert Syst. Appl. 40 (18), 7407–7414. Han, O., Liu, X., Xu, J., 2022. Detection and location of steel structure surface cracks based on unmanned aerial vehicle images. J. Build. Eng. 50, 104098.
- Housner, G.W., 1952. Spectrum intensities of strong-motion earthquakes.
- Indirli, M., S. Kouris, L.A., Formisano, A., Borg, R.P., Mazzolani, F.M., 2013. Seismic damage assessment of unreinforced masonry structures after the Abruzzo 2009 earthquake: The case study of the historical centers of L'Aquila and Castelvecchio Subequo. Int. J. Archit. Herit. 7 (5), 536–578.
- Ji, M., Liu, L., Buchroithner, M., 2018. Identifying collapsed buildings using post-earthquake satellite imagery and convolutional neural networks: A case study of the 2010 Haiti earthquake. Remote Sens. 10 (11), 1689.
- Kong, D., Chen, Y., Li, N., 2018. Gaussian process regression for tool wear prediction. Mech. Syst. Signal Process. 104, 556-574.
- Kourehpaz, P., Molina Hutt, C., 2022. Machine learning for enhanced regional seismic risk assessments. J. Struct. Eng. 148 (9), 04022126.
- Kovačević, M., Stojadinović, Z., Marinković, D., Stojadinović, B., 2018. Sampling and machine learning methods for a rapid earthquake loss assessment system. In: 11th US National Conference on Earthquake Engineering. Earthquake Engineering Research Institute, Los Angeles, CA.
- Kundu, T., Sheu, J.-B., Kuo, H.-T., 2022. Emergency logistics management—Review and propositions for future research. Transp. Res. E 164, 102789.
- Laganà, D., Laporte, G., Vocaturo, F., 2021. A dynamic multi-period general routing problem arising in postal service and parcel delivery systems. Comput. Oper. Res. 129, 105195.
- Lagaros, N.D., Karlaftis, M.G., 2011. A critical assessment of metaheuristics for scheduling emergency infrastructure inspections. Swarm Evol. Comput. 1 (3), 147–163.
- Larrain, H., Coelho, L.C., Archetti, C., Speranza, M.G., 2019. Exact solution methods for the multi-period vehicle routing problem with due dates. Comput. Oper. Res. 110, 148–158.
- Levine, N.M., Spencer, Jr., B.F., 2022. Post-earthquake building evaluation using UAVs: A BIM-based digital twin framework. Sensors 22 (3), 873.
- Li, L., Ma, Z., Bensi, M., Baecher, G.B., 2023. Social media crowdsourcing for earthquake damage assessment. In: Geo-Risk 2023. pp. 161-170.
- Liu, K., Hu, X., Wei, Z., Li, Y., Jiang, Y., 2019. Modified Gaussian process regression models for cyclic capacity prediction of lithium-ion batteries. IEEE Trans. Transp. Electr. 5 (4), 1225–1236.
- Liu, Z., Jiang, X., Luo, H., Fang, W., Liu, J., Wu, D., 2021. Pool-based unsupervised active learning for regression using iterative representativeness-diversity maximization (iRDM). Pattern Recognit. Lett. 142, 11–19.
- Liu, Z., Wu, D., 2020. Integrating informativeness, representativeness and diversity in pool-based sequential active learning for regression. In: 2020 International Joint Conference on Neural Networks. IJCNN, IEEE, pp. 1–7.
- Lu, X., Guan, H., 2017. Earthquake Disaster Simulation of Civil Infrastructures. Springer.
- Lu, X., McKenna, F., Cheng, Q., Xu, Z., Zeng, X., Mahin, S.A., 2020. An open-source framework for regional earthquake loss estimation using the city-scale nonlinear time history analysis. Earthq. Spectra 36 (2), 806–831.
- Ma, H., Liu, Y., Ren, Y., Wang, D., Yu, L., Yu, J., 2020. Improved CNN classification method for groups of buildings damaged by earthquake, based on high resolution remote sensing images. Remote Sens. 12 (2), 260.
- Madichetty, S., Sridevi, M., 2019. Disaster damage assessment from the tweets using the combination of statistical features and informative words. Soc. Netw. Anal. Min. 9, 1–11.
- Mangalathu, S., Jeon, J.-S., 2020. Regional seismic risk assessment of infrastructure systems through machine learning: Active learning approach. J. Struct. Eng. 146 (12), 04020269.
- Mangalathu, S., Sun, H., Nweke, C.C., Yi, Z., Burton, H.V., 2020. Classifying earthquake damage to buildings using machine learning. Earthq. Spectra 36 (1), 183–208.
- Nagasawa, R., Mas, E., Moya, L., Koshimura, S., 2021. Model-based analysis of multi-UAV path planning for surveying postdisaster building damage. Sci. Rep. 11 (1), 18588.
- Neves-Moreira, F., Amorim-Lopes, M., Amorim, P., 2020. The multi-period vehicle routing problem with refueling decisions: Traveling further to decrease fuel cost? Transp. Res. E 133, 101817.
- Oruc, B.E., Kara, B.Y., 2018. Post-disaster assessment routing problem. Transp. Res. B 116, 76-102.
- Petersson, N., Sjogreen, B., 2017. SW4, Version 2.01 [Software]. Computational Infrastructure of Geodynamics. Vol. 10, Zenodo, Switzerland, p. 5281.
- Qin, H., Ming, W., Zhang, Z., Xie, Y., Lim, A., 2015. A tabu search algorithm for the multi-period inspector scheduling problem. Comput. Oper. Res. 59, 78–93. Qing, Y., Ming, D., Wen, Q., Weng, Q., Xu, L., Chen, Y., Zhang, Y., Zeng, B., 2022. Operational earthquake-induced building damage assessment using CNN-based direct remote sensing change detection on superpixel level. Int. J. Appl. Earth Obs. Geoinf. 112, 102899.
- Quitoriano, V., Wald, D.J., 2020. USGS "Did You Feel It?"—Science and lessons from 20 years of citizen science-based macroseismology. Front. Earth Sci. 8, 120.
- Rathje, E.M., Dawson, C., Padgett, J.E., Pinelli, J.-P., Stanzione, D., Adair, A., Arduino, P., Brandenberg, S.J., Cockerill, T., Dey, C., et al., 2017. DesignSafe: New cyberinfrastructure for natural hazards engineering. Nat. Hazards Rev. 18 (3), 06017001.
- Rodgers, A.J., Pitarka, A., Pankajakshan, R., Sjögreen, B., Petersson, N.A., 2020. Regional-scale 3D ground-motion simulations of Mw 7 earthquakes on the Hayward fault, northern California resolving frequencies 0–10 Hz and including site-response corrections. Bull. Seismol. Soc. Am. 110 (6), 2862–2881.
- Sadeghi, A., Aros-Vera, F., Mosadegh, H., YounesSinaki, R., 2023. Social cost-vehicle routing problem and its application to the delivery of water in post-disaster humanitarian logistics. Transp. Res. E 176, 103189.
- Schulz, E., Speekenbrink, M., Krause, A., 2018. A tutorial on Gaussian process regression: Modelling, exploring, and exploiting functions. J. Math. Psych. 85, 1–16.
- Sheibani, M., Ou, G., 2021. The development of Gaussian process regression for effective regional post-earthquake building damage inference. Comput.-Aided Civ. Infrastruct. Eng. 36 (3), 264–288.

Sheibani, M., Wang, Y., Ou, G., Marković, N., 2022. Efficient structural reconnaissance surveying for regional postseismic damage inference with optimal inspection scheduling. J. Eng. Mech. 148 (2), 04021156.

Stojadinović, Z., Kovačević, M., Marinković, D., Stojadinović, B., 2022. Rapid earthquake loss assessment based on machine learning and representative sampling.

Sun, A.Y., Wang, D., Xu, X., 2014. Monthly streamflow forecasting using Gaussian process regression. J. Hydrol. 511, 72-81.

Tamang, T., Ramtel, P., Thapa, S., Thapa, D., Bhattarai, P., Shrestha, J.K., 2023. Qualitative evaluation of reconstructed masonry residential building after the Gorkha earthquake 2015 in rural areas of Nepal: A case study at Bhalche, Nuwakot. J. Inst. Eng. 17 (1), 38–52.

Vincent, F.Y., Jewpanya, P., Lin, S.-W., Redi, A.P., 2019. Team orienteering problem with time windows and time-dependent scores. Comput. Ind. Eng. 127, 213–224

Waddell, P., 2002. UrbanSim: Modeling urban development for land use, transportation, and environmental planning. J. Am. Plan. Assoc. 68 (3), 297-314.

Wang, Y., Cui, L., Zhang, C., Chen, W., Xu, Y., Zhang, Q., 2022. A two-stage seismic damage assessment method for small, dense, and imbalanced buildings in remote sensing images. Remote Sens. 14 (4), 1012.

Wang, Y., Jing, X., Cui, L., Zhang, C., Xu, Y., Yuan, J., Zhang, Q., 2023b. Geometric consistency enhanced deep convolutional encoder-decoder for urban seismic damage assessment by UAV images. Eng. Struct. 286, 116132.

Wang, Y., Jing, X., Xu, Y., Cui, L., Zhang, Q., Li, H., 2023c. Geometry-guided semantic segmentation for post-earthquake buildings using optical remote sensing images. Earthq. Eng. Struct. Dyn. 52 (11), 3392–3413.

Wang, J., Xie, W., Ryzhov, O.I., Marković, N., Ou, G., 2023a. D-optimal orienteering for post-earthquake reconnaissance planning. In revision at Operations Research.

Wieland, M., Pittore, M., Parolai, S., Zschau, J., Moldobekov, B., Begaliev, U., 2012. Estimating building inventory for rapid seismic vulnerability assessment: Towards an integrated approach based on multi-source imaging. Soil Dyn. Earthq. Eng. 36, 70–83.

Williams, C.K., Rasmussen, C.E., 2006. Gaussian Processes for Machine Learning, Vol. 2, MIT press Cambridge, MA.

Wu, D., 2018. Pool-based sequential active learning for regression. IEEE Trans. Neural Netw. Learn. Syst. 30 (5), 1348-1359.

Wu, H., Cheng, Z., Shi, W., Miao, Z., Xu, C., 2014. An object-based image analysis for building seismic vulnerability assessment using high-resolution remote sensing imagery. Nat. Hazards 71, 151–174.

Wu, R., Wang, B., 2018. Gaussian process regression method for forecasting of mortality rates. Neurocomputing 316, 232-239.

Xia, H., Wu, J., Yao, J., Zhu, H., Gong, A., Yang, J., Hu, L., Mo, F., 2023. A deep learning application for building damage assessment using ultra-high-resolution remote sensing imagery in Turkey earthquake. Int. J. Disaster Risk Sci. 14 (6), 947–962.

Xing, Z., Zhang, X., Zan, X., Xiao, C., Li, B., Han, K., Liu, Z., Liu, J., 2021. Crowdsourced social media and mobile phone signaling data for disaster impact assessment: A case study of the 8.8 Jiuzhaigou earthquake. Int. J. Disaster Risk Reduct. 58, 102200.

Xiong, C., Li, Q., Lu, X., 2020. Automated regional seismic damage assessment of buildings using an unmanned aerial vehicle and a convolutional neural network. Autom. Constr. 109, 102994.

Xu, Y., Li, Y., Zheng, X., Zheng, X., Zhang, Q., 2023a. Computer-vision and machine-learning-based seismic damage assessment of reinforced concrete structures. Buildings 13 (5), 1258.

Xu, Y., Qiao, W., Zhao, J., Zhang, Q., Li, H., 2023b. Vision-based multi-level synthetical evaluation of seismic damage for RC structural components: a multi-task learning approach. Earthq. Eng. Vib. 22 (1), 69–85.

Xu, Y., Wei, S., Bao, Y., Li, H., 2019. Automatic seismic damage identification of reinforced concrete columns from images by a region-based deep convolutional neural network. Struct. Control Health Monit. 26 (3), e2313.

Zeng, A., Ho, H., Yu, Y., 2020. Prediction of building electricity usage using Gaussian process regression. J. Build. Eng. 28, 101054.

Zeng, X., Lu, X., Yang, T., Xu, Z., 2016. Application of the FEMA-P58 methodology for regional earthquake loss prediction. Nat. Hazards 83, 177-192.

Zhang, J., Li, Y., Lu, Z., 2024. Multi-period vehicle routing problem with time windows for drug distribution in the epidemic situation. Transp. Res. C 160, 104484.

Zsarnóczay, A., Elhaddad, W., Cetiner, B., Zhong, K., McKenna, F., Deierlein, G., 2023. SimCenter Earthquake Testbed. DesignSafe-CI, San Francisco, CA.